

# Compare Results

Old File:

**main\_manuscript\_old\_compressed.pdf**

**39 pages (3.11 MB)**

2/15/22, 19:18:06

versus

New File:

**main\_manuscript\_final\_compressed.pdf**

**41 pages (2.11 MB)**

2/15/22, 19:30:04

## Total Changes

**1400**

## Content

876 Replacements  
254 Insertions  
243 Deletions

## Styling and Annotations

27 Styling  
0 Annotations

[Go to First Change \(page 1\)](#)

# Elevation Change of the Antarctic Ice Sheet: 1985 to 2020

Johan Nilsson<sup>1</sup>, Alex S. Gardner<sup>1</sup> and Fernando S. Paolo<sup>1</sup>

<sup>1</sup> Jet Propulsion Laboratory, California Institute of Technology, Pasadena, 91109, United States

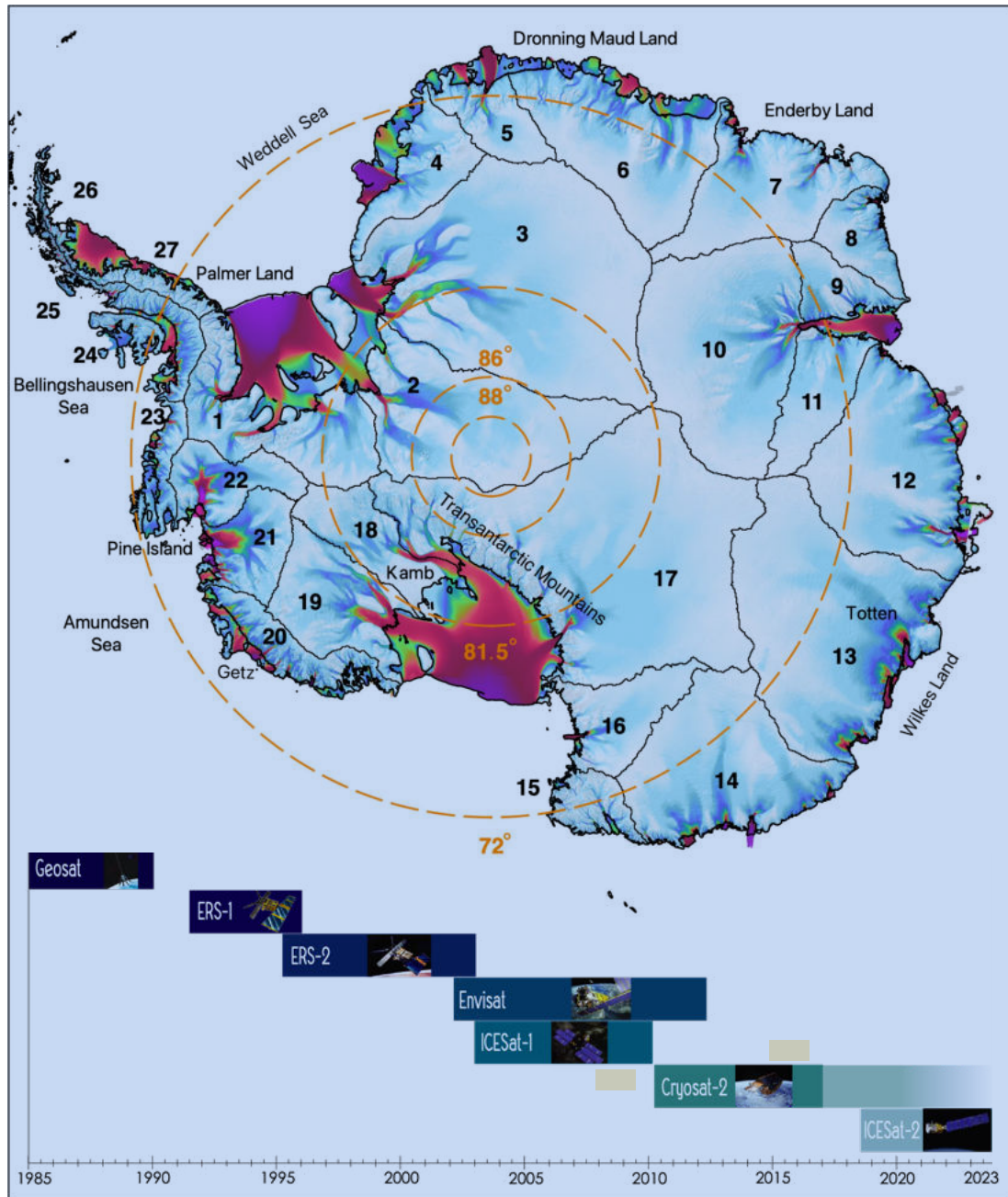
*Correspondence to:* Johan Nilsson (johan.nilsson@jpl.nasa.gov)

## Abstract.

The largest uncertainty in future projections of sea level change comes from the uncertain response of the Antarctic Ice Sheet to the warming oceans and atmosphere. The ice sheet gains roughly 2000 km<sup>3</sup> of ice from precipitation each year and loses a similar amount through solid ice discharge into the surrounding oceans. Numerous studies have shown that the ice sheet is currently out of long-term equilibrium, losing mass at an accelerated rate and increasing sea level rise. Projections of sea-level change rely on accurate estimates of the contribution of land ice to the contemporary sea level budget. The longest observational record available to study the mass balance of the Earth's ice sheets comes from satellite altimeters. This record, however, consists of multiple satellite missions with different life-spans, inconsistent measurement types (radar and laser) and of varying quality. To fully utilize these data, measurements from different missions must be cross-calibrated and integrated into a consistent record of change. Here, we present a novel approach for generating such a record that implies improved topography removal, cross-calibration and normalization of seasonal amplitudes from different mission. We describe in detail the advanced geophysical corrections applied and the processes needed to derive elevation change estimates. We processed the full archive record of satellite altimetry data, providing a seamless record of elevation change for the Antarctic Ice Sheet that spans the period 1985 to 2020. The data are produced and distributed as part of the NASA MEaSUREs ITS\_LIVE project (Nilsson et al., 2021, DOI: <https://doi.org/10.5067/L3LSVDZS15ZV>).

## 38 1 Introduction

39 The single largest uncertainty in multi-centennial projections of sea level change comes from the uncertain  
40 response of the Antarctic Ice Sheet to warming oceans and atmosphere (Oppenheimer et al, 2019). Reductions in  
41 uncertainty will come primarily from developing our understanding of the ice sheet’s response to changes in ocean  
42 and atmosphere over the observational record. Given the inaccessibility and size of the ice sheet, satellite  
43 observations provide the most comprehensive means to assess ice sheet change. One of the most valued  
44 observational records comes from a handful of satellite altimeters that, in combination, provide a near-continuous  
45 record of elevation-change from 1992 (McMillan et al., 2014; Schröder et al., 2019; Shepherd et al., 2018, 2019;  
46 Zwally et al., 2015, 2021). These observations have provided invaluable insights into how the topography of  
47 Antarctica has changed over the past 30 years, revealing rapid thinning of key West Antarctic glaciers (Konrad et  
48 al., 2017) that have the potential to thin and retreat irreversibly (Joughin et al., 2014; Rignot et al., 2014). Previous  
49 studies of the polar ice sheets that used data from a single satellite mission have been hampered by relatively short  
50 records over which to assess change. Records longer than 10 to 20 years are needed to reduce the overall  
51 uncertainty in elevation change assessments and to reduce the impact of short-term variability on the climate  
52 series (Wouters et al., 2013). Therefore, the creation of long-term records is essential for the separation of **short-**  
53 **term** variability from long-term change. Such records require piecing together observations from numerous  
54 satellite instruments, with unique measurement characteristics and sources of error. Previous studies have tried to  
55 overcome these issues by either comparing **inter-mission** rates of elevation change (avoiding merging the records)  
56 or merging the records at relatively coarse resolution (>50 km) (Davis, 2000; Khvorostovsky, 2012). More  
57 recently, progress has been made to construct synthesized records of ice sheet elevation at higher resolution  
58 (Schröder et al., 2019; Shepherd et al., 2019; Wingham et al., 2006). Many issues still remain unsolved, including  
59 the proper accounting of radar-penetration, slope induced errors, and resolving time-variable and static  
60 topography. In this study, we provide new and modified algorithms to mitigate the impact of these issues on the  
61 elevation change record. In support of the “Inter-mission Time Series of Land Ice Velocity and Elevation”  
62 (ITS\_LIVE), a “NASA Making Earth System Data Records for Use in Research Environments” (MEaSUREs)  
63 project, we revisit the processing and cross-calibration of more than 30 years of altimetry measurements over  
64 Antarctica to provide a state-of-the-art climate record of ice sheet topographic change. Specifically, we combine  
65 data from four conventional pulse-limited radar altimeters (Geosat, ERS-1, ERS-2, and Envisat), a dual antenna  
66 radar altimeter capable of operating in both Synthetic Aperture Radar Interferometric mode and pulse-limited  
67 mode (CryoSat-2), and a small-footprint waveform (ICESat) and photon counting (ICESat-2) laser altimeters,  
68 yielding the most comprehensive record of Antarctic elevation change to date (Figure 1).



69 Figure 1: Spatial and temporal coverage of the seven satellite altimetry missions used to produce the elevation  
 70 change synthesis. Concentric dashed circles and labels (orange) indicate orbital limits of each mission (Geosat  
 71 72° ERS-1/2 and Envisat – 81.5°, ICESat 86° and CryoSat-2/ICESat-2 88°). Antarctic drainage basins 1-27 are  
 72 show in black (Zwally et al., 2012). Orbital limits and drainage basins are plotted over ITS\_LIVE velocities  
 73 (Gardner et al., 2018) merged with the inSAR phase-based estimates (Mouginot et al., 2019).  
 74  
 75  
 76

## 77 2 Data

### 78 2.1 Geosat

79 The U.S Navy launched the GEODETIC SATellite (Geosat) in March 1985, which operated until September 1989,  
80 providing limited Antarctic coverage between  $\pm 72^\circ$  latitude. The main goal of the mission was to provide the U.S  
81 Navy with detailed information about the marine gravity field. Geosat operations consisted of two separate  
82 missions, where the initial 18 months was the classified “Geodetic Mission” (GM), in a 135-day repeat orbit,  
83 ending in September 1986, and the “Exact Repeat Mission” (ERM), in a 17-day repeat orbit, lasting until the end  
84 of the mission. The mission carried a Ku-band (13.5 GHz) pulse-limited altimeter providing measurements every  
85 670 m along-track (10 Hz), with a pulse-limited diameter of  $\sim 3$  km. In this study we used “Ice Data Record”  
86 (IDR) from the Radar Ice Altimetry Group at NASA Goddard Space Flight Center (GSFC) providing geolocated  
87 and corrected surface elevations. Only records with a valid retracking correction and waveforms containing a  
88 single return echo were used in the study to reduce noise in the derived surface elevations. We detected the  
89 presence of a bias in the Automatic Gain Control (AGC) parameter of 1.23 dB between the Geodetic Mission  
90 (GM) and the Exact Repeat Mission (ERM) phases. This is most likely due to the change in orbit and did not  
91 affect any of the other parameters, including the surface elevation change.

### 92 2.2 ERS-1 and ERS-2

93 The European Space Agency (ESA) launched the European Remote Sensing (ERS) satellites in 1991 (ERS-1) and  
94 1995 (ERS-2) respectively. They operated continuously between  $\pm 81.5^\circ$  latitude until 1996 and 2003,  
95 respectively. Both missions carried conventional pulse-limited Ku-band (13.6 GHz) radar altimeters, with a pulse-  
96 limited footprint of  $\sim 1.5$  km, and an along track resolution of 370 m (20 Hz sampling rate). The two missions  
97 operated in a 35-day repeat orbit, though ERS-1 had several shorter mission phases early on that deviated from  
98 the standard repeat-track orbit. For this study the “REprocessing of Altimeter Products for ERS (GDR): 1991 to  
99 2003” (REAPER), detailed in Brockley et al. (2017) is used to obtain surface elevation measurements. This  
100 product contains updated corrections and improved calibrations. For each satellite record we separated the data  
101 from the two operational modes, ‘ocean’ and ‘ice’, excluding any data used for calibration. The product provides  
102 different retracking solutions from which we have chosen to use the ICE1 retracker, otherwise known as the  
103 “Offset Center of Gravity” (OCOg) retracker (Wingham et al., 1986) using a 30% threshold of the maximum  
104 waveform amplitude. The Ku-chirp and the ICE-1 20 Hz quality flags, available in the product, were used to  
105 exclude poor quality observations from the analysis.

### 106 2.3 Envisat

107 The “Environmental Satellite” (Envisat) was launched by ESA in 2002 as a successor to the ERS mission and was  
108 officially decommissioned in 2012. Envisat was launched into a 35-day repeat orbit, operating with a pulse-limited  
109 radar altimeter with the same footprint, radar frequency, and sample frequency as the earlier ERS missions. For  
110 Envisat we used the “RA-2 Geophysical Data Record” (GDR) version 2.1. Only data collected during the period  
111 2002 to 2010 were used due to changes in orbit initiated in October of 2010. The GDR product, as with the  
112 REAPER product, includes elevations determined using the ICE-1 retracker with a 30% threshold of the

113 maximum waveform amplitude, which we used for this analysis. We applied the same quality filter on the GDR  
114 records as with the ERS product, using the Ku-chip and ICE-1 quality flags.

## 115 2.4 ICESat and ICESat-2

116 The National Aeronautics and Space Administration (NASA) launched the Ice, Cloud, and land Elevation Satellite  
117 (ICESat) in 2003, which operated from 2003 to 2009, in a 96-day repeat orbit. The mission carried a novel laser  
118 altimeter providing a 70 m beam-limited ground footprint, with 170 m along-track sampling (40 Hz). We used  
119 the latest version of the GLAS06 product (release 34), which has been corrected for the “Gaussian-Centroid-  
120 Offset” (Borsa et al., 2014), detector saturation and converted to heights above the WGS84 ellipsoid. We did not  
121 apply any inter-campaign bias to the ICESat elevations, as there is no consensus that these are required (Borsa et  
122 al., 2019). The records are further edited to remove poor quality observations, using the accompanying quality  
123 flags ( $\text{elev\_use\_flh} > 0$ ,  $\text{sat\_corr\_flg} > 2$ ,  $\text{sigma\_att\_flg} > 0$ ,  $\text{i\_numPk} > 0$ ).

124  
125 The ICESat-2 mission is a follow on mission to ICESat and was launched in October 2018 with the goal of  
126 continuing the long-term altimetry measurements of polar regions (Markus et al., 2017). It carries a new and novel  
127 photon counting laser altimeter that uses a 532 nm laser with a pulse repetition rate of 10 kHz and that operates  
128 in a repeat-track configuration over the continental ice sheets. In contrast to its predecessor’s single beam, ICESat-  
129 2 collects ground measurements using six individual laser beams arranged in three pairs. Each of the beam pairs  
130 is separated by 3 km and each inter-pair beam by 90 m across track. This configuration allows for a direct estimate  
131 of the across track surface slope that was not directly possible with ICESat’s single beam configuration. The beam  
132 limited footprint for each beam is 12 m in diameter sampling every 0.7 m along-track with a repeat frequency of  
133 91 days. In this study surface elevation from the ATL06 product was used following the approach outlined in  
134 Smith et al. (2019, 2020). Here a segmentation filter (difference filter) was used to remove poor quality  
135 observations, if differences between consecutive points exceeds a threshold of 2 m the point was rejected. Further  
136 editing was done using the ATL06 quality flag, keeping only data designated to be of good quality  
137 (“*atl06\_quality\_summary* = 0”).

## 138 2.5 CryoSat-2

139 ESA’s CryoSat-2 mission launched in 2010 with the primary purpose of monitoring changes in Earth’s Sea and  
140 land ice. This satellite carries a new type of Doppler/delay radar altimeter (Raney, 1998) equipped with a dual  
141 antenna configuration allowing for interferometric measurements of surface elevations. The altimeter system,  
142 referred to as SIRAL, operates in two different modes over the ice sheets; a Synthetic Aperture Radar  
143 Interferometric (SARIn) mode over the marginal areas and a Low-Resolution Mode (LRM) [a conventional Ku-  
144 band pulse-limited radar (identical to ERS and Envisat)] over the ice sheet interiors. The Doppler/delay radar  
145 allows for increased along-track resolution compared to conventional pulse-limited altimetry. The SARIn-mode  
146 has an effective resolution of 350 m along-track and 1500 m across-track, compared to the LRM-modes 1500 m  
147 along and across track resolution. Further, the dual antenna configuration allows for mapping of the exact position  
148 of the surface echo location, by estimation of the across-track look angle<sup>\*</sup> from the difference in path length of the  
149 signals between the two antennas. In contrast to previous missions,<sup>\*</sup> CryoSat-2 operates in a drifting orbit, with a  
150 369-day repeat and a 30-day sub-cycle. The drifting orbit offers<sup>\*</sup> improved spatial coverage compared to repeat-

151 track orbits at the expense of larger across track distances. We processed both the LRM and SARIn modes using  
152 the ESA L1b Baseline-C product for the time span 2010-2018 using a custom CryoSat-2 processor described in  
153 Nilsson et al. (2016). For the LRM-mode we have chosen to use a 10% threshold of the maximum waveform  
154 amplitude for retracking, similar to Schröder et al., (2019).

### 155 3 Methods

156 To generate a continuous record of elevation change for Antarctica several corrections and processing steps need  
157 to be applied to the altimetry data. The details of the different steps are provided in this section and a summary of  
158 the corrections their order of application is provided below:

- 159 1. Application of geophysical corrections and parameter editing for each mission [Section 2].
- 160 2. Correcting for slope-induced error in the radar altimetry using an ancillary elevation model [Section  
161 3.1].
- 162 3. Removal of the static topography to extract time-variable elevation change [Section 3.2.1].
- 163 4. Correcting the radar altimetry data for changes in near-surface scattering conditions [Section 3.2.2].
- 164 5. Cross-calibration and integration of the multiple sensors and modes into a continuous time series  
165 [Section 3.2.3].
- 166 6. Normalization of seasonal amplitudes for each sensor using a reference mission [Section 3.2.4].
- 167 7. Interpolation, extrapolation and filtering to create a three-dimensional data product [Section 3.2.5].

#### 168 3.1 Slope-induced error correction

169 The largest source of error in radar altimetry over ice sheets is associated with the effects of surface slope inside  
170 the beam-limited radar footprint. This error stems from an inability to locate the surface from which most of the  
171 echo power originates (off Nadir). Because of this, the echo is assigned the location of the sub-satellite point on  
172 the Earth surface. This introduces a slope-dependent measurement error on the order of 0-100 m (Brenner et al.,  
173 1983), which varies with the magnitude of the surface slope. There are a few ways of minimizing the slope-  
174 induced error (Bamber, 1994; Roemer et al., 2007). For this study we used the “relocation method” described in  
175 (Nilsson et al., 2016). The relocation method corrects both the range and the coordinates to the echolocation (from  
176 nadir) using topographical information, such as surface slope, aspect and curvature. This method has been shown  
177 to improve surface-elevation retrievals compared to other approaches (e.g. Schröder et al., 2017). To compute the  
178 required surface slope, aspect and curvature, we used the “bedmap2” digital elevation model from Fretwell et al.  
179 (2013) resampled to 2 km horizontal resolution.

#### 180 3.2 Elevation change estimation and algorithms

181 Surface elevation changes are determined as follows: The local mean topography within a specified search radius  
182 is removed from each mission and mode, leaving only the elevation anomalies that contain the time variable  
183 signal. Artificial trends and seasonal amplitudes in elevation anomalies, that are introduced by changes in surface  
184 scattering characteristics, are reduced proportionally to the correlation with the received radar waveform shape.  
185 Inter-mission biases in seasonal elevation anomalies are further minimized using a normalization scheme that  
186 references all seasonal elevation change amplitudes to those observed by CryoSat-2. A cross-calibration scheme

187 is applied to adjust and merge elevation change from all missions and modes into a continuous monthly time  
188 series. Lastly, interpolation is used to generate a consistent gridded product with 1920 m horizontal resolution at  
189 monthly time steps from 1985 to 2020. The details of each step are provided in the following sub-sections.

### 190 3.2.1 Removal of time-invariant topography

191 To create time series from observations of surface elevations, the time-invariant topography must be removed to  
192 obtain the change signal. This can be done by directly modelling the topography at any given position, e.g., by  
193 fitting a mathematical surface using least-squares, while accounting for the spatial and temporal trends. This rather  
194 simple approach, however, has some inherent limitations. When solving for time-invariant topography one must  
195 account for discrepancies between observations originating from: (1) differences in the orbital geometry of the  
196 missions, (2) differences in ascending versus descending range estimates and (3) differences in measurement  
197 density. To account for (1) we employ an iterative prediction-point adjustment to solve for the topography given  
198 a pre-defined grid of a specified dimension for ascending and descending tracks separately for each mission or  
199 mode. For each grid-node, the closest data points inside a specified search radius are used to compute a new  
200 centroid location, when 5 or more data points are available. This centroid location is used in the next iteration as  
201 the new prediction point. This allows us to conveniently follow the reference orbits (locations of highest data  
202 density) to solve for the topography along the satellite ground tracks. Issue (2) has been handled in different ways  
203 (e.g., Flament et al., 2012; McMillan et al., 2014; Moholdt et al., 2010). We have chosen to solve (2) by separating  
204 the individual datasets in ascending and descending orbits, solving for the topography at the same center date with  
205 the inclusion of a linear trend. The differing number of available observations (3) in each independent solution is  
206 handled by allowing for a different number of coefficients in the mathematical surface-topography model that is  
207 fit to the data. We have provided three different mathematical models of topography (including time) that vary  
208 spatially depending on the number of data points available in the local search area at the grid-node.

209 For locations with 15 or more observations a biquadratic surface (six coefficients) is modeled. When 5 to 14  
210 observations are available a bilinear surface (three coefficients) is modeled. If there are less than 5 observations  
211 the local mean (one coefficient) is removed and the slopes estimated independently in each direction ( $x$  and  $y$ ).  
212 The linear temporal term in the design matrix is used to center the data to a specific time and is always included,  
213 except if  $n < 5$  points. A robust least squares approach, M-estimator (Hubert' T weighting function), is used to  
214 solve for the model coefficients (Holland et al., 1977).

215  
216 Time-invariant surface topography is estimated at each prediction point and removed from the original  
217 observations inside each local search radius (excluding the linear term). This produces topographic residuals  
218 varying only with time. Using this approach, it is common for the search radius of different along-track centroids  
219 to overlap. This can produce situations where a node, with corresponding elevation data, might already have been  
220 provided with a solution. To ensure that the best time-invariant topography solution is retained, the new correction  
221 is only applied if the estimated root-mean-square (RMS) of the residuals (w.r.t. the time-invariant topography) is  
222 lower than the previously computed solution for the data point in question.

223

224



225 We select different search-radii for the repeat-track (ERS 1/2, Envisat, ICESat, Geosat) and drifting-track  
 226 (CryoSat-2) missions. The radius is empirically determined by investigating the residual RMSE from the  
 227 algorithm over different types of surfaces. We found that, on a 500 m grid spacing, a search radius of 500 m  
 228 provided a good trade-off between the accuracy and computational efficiency of the algorithm for the repeat-track  
 229 missions. For CryoSat-2 and Geosat, we found that a higher search radius of 1000 m was needed to provide results  
 230 with a comparable RMSE. This larger search radius allows for more ground tracks to be included in the inversion,  
 231 reducing the variance of the model residuals. The inclusion of a linear temporal trend in the fit is key to effectively  
 232 remove the ascending/descending bias, and to center all data to a common epoch (center date of each mission or  
 233 mode).

### 234 3.2.2 Surface and volume scattering correction

235 The microwave pulses transmitted by spaceborne radar altimeters at Ku-band frequency (~13.6 GHz) are sensitive  
 236 to changes in the dielectric properties of the ice sheet surface (as determined by changes in the snow grain size,  
 237 temperature, density, water content, among others). Large scale temporal and spatial changes in the scattering  
 238 horizon induce changes in measured range, and thus surface elevation, and can introduce long-lived biases in the  
 239 derived elevation change rates (Arthern et al., 2001; Davis et al., 2004; Khvorostovsky, 2012; Nilsson et al., 2015;  
 240 Wingham et al., 1998). To mitigate this effect, we use a retracking algorithm that tracks the leading edge of the  
 241 return waveform (i.e., a maximum amplitude threshold between 10% and 30%). Such retrackers have been shown  
 242 to be less sensitive to changes in ice sheet surface properties (Helm et al., 2014; Nilsson et al., 2016; Schröder et  
 243 al., 2017). Another key step is removing elevation variability that is correlated with changes in the received radar  
 244 waveform shape (Flament and Rémy, 2012; McMillan et al., 2014; Paolo et al., 2016; Simonsen et al., 2017;  
 245 Zwally et al., 2005). The shape of the waveform is intricately linked to the medium in which it is propagated or  
 246 reflected. Removing the correlation between changes of the shape of the radar waveform with elevation can  
 247 largely reduce these artificial signals. For this study we approximated the shape of the radar waveform following  
 248 the definition of Flament et al., (2012) and Simonsen et al., (2017), using the backscatter (Bs), the leading-edge  
 249 width (LeW) and the trailing edge slope (TeS).

250  
 251 The spatially-variant scattering correction was estimated by computing the local sensitivity gradient (SG) between  
 252 each waveform parameter and elevation residuals using a multi-variate least squares inversion. The SG-  
 253 parameters were estimated for ascending and descending tracks separately. All waveform parameter time series  
 254 were centered and normalized using the mean and standard deviation. Further, parameters were detrended by  
 255 applying a difference operator, forming the following least-squares model:

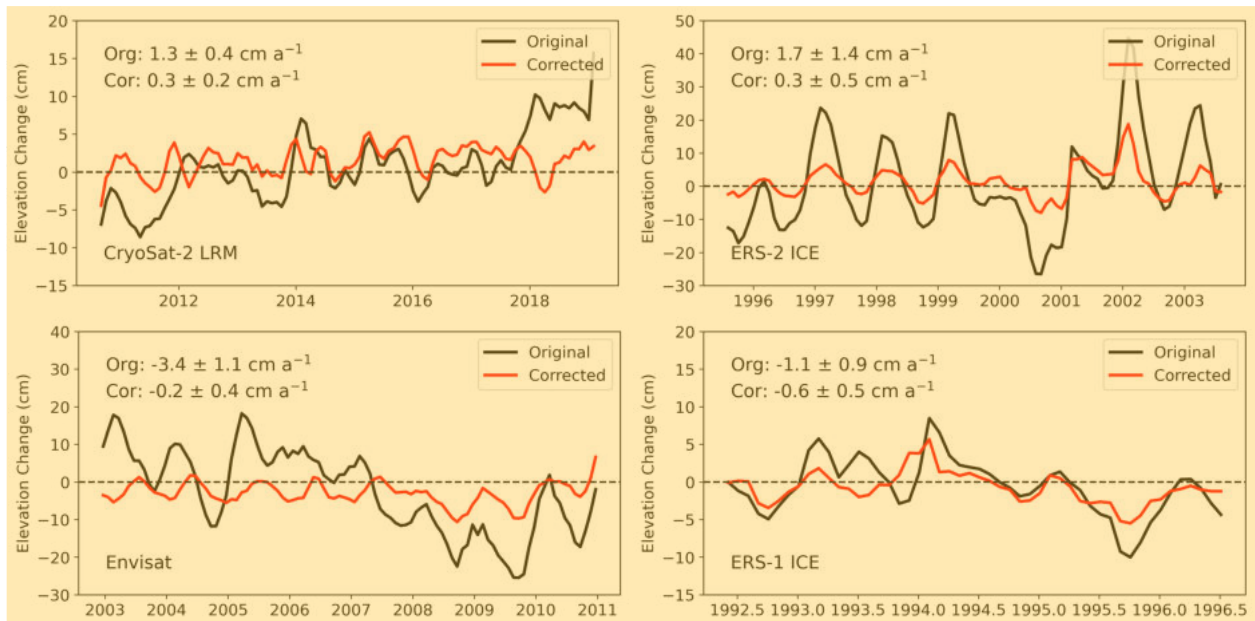
$$\nabla \left( \frac{h - \bar{h}}{\sigma_{dh}} \right) = SG_{Bs} \cdot \nabla \left( \frac{s - \bar{Bs}}{\sigma_{Bs}} \right) + SG_{LeW} \cdot \nabla \left( \frac{eW - \bar{LeW}}{\sigma_{LeW}} \right) + SG_{TeS} \cdot \nabla \left( \frac{eS - \bar{TeS}}{\sigma_{TeS}} \right) \quad (1)$$

256  
 257 where  $\nabla$  is the difference operator,  $h$  the elevation residual (elevation relative to time-invariant topography),  $\sigma$  the  
 258 standard deviation and the overbar represents the average value of the parameter.

259

260

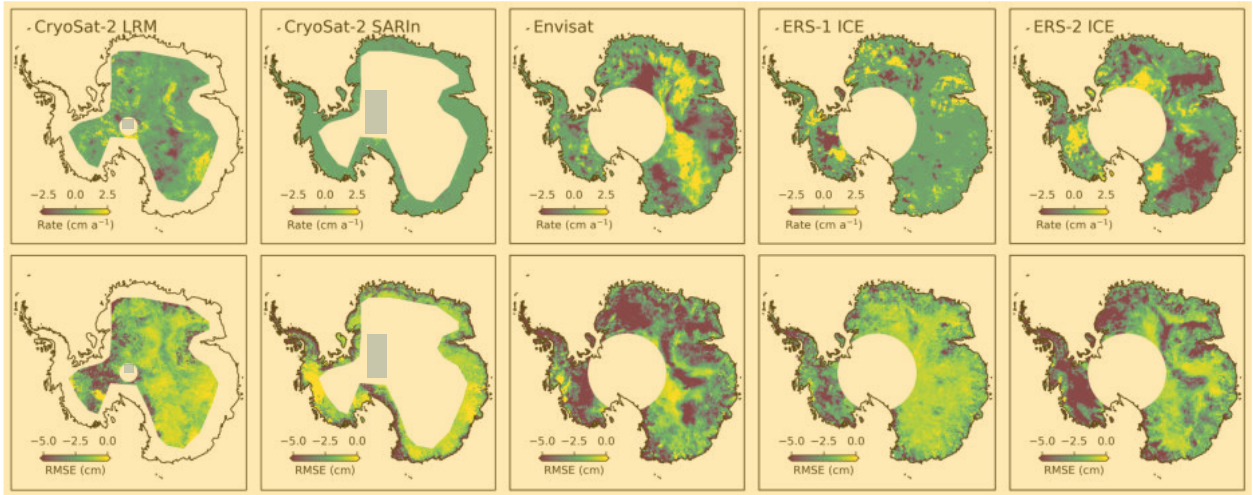
261 The SG-parameters were inverted for using the same adaptive search-center approach as described in Sect. 3.2.1.  
 262 The estimated SGs were then used to correct each observation within the search cap using the linear combination  
 263 of the original waveform parameters and the estimated coefficients. Finally, we apply a linear space-time  
 264 interpolation to estimate corrections at locations where the multi-variate fit did not provide a satisfactory solution.  
 265



266  
 267 Figure 2. Original and scattering corrected time series for Lake Vostok in East Antarctica, which has been shown  
 268 to have a height trend close to zero over recent decades (Richter et al., 2014). A discrepancy in uncorrected height  
 269 trends is observed for the various mission due to differences in altimetry processing, orbit configuration and the  
 270 quality of the geophysical corrections. Envisat and ERS-2 (Ice) show the largest uncorrected magnitude in both  
 271 trend and seasonal signal. Corrected height change records show significantly lower seasonal amplitudes and  
 272 trends that are close to zero.

273  
 274 To determine the optimal search radius for generating the scattering correction, we performed a sensitivity study  
 275 over Lake Vostok in East Antarctica (Figure 2). Lake Vostok was selected due to its low surface slope, on average  
 276  $0.03^\circ$ , and highly stable surface (Richter et al., 2014), minimizing the impact of the static and time variable  
 277 topography in the analysis. After varying the search radius from 1 to 5 km, we found that the 1 km solution  
 278 provided the most accurate trend and seasonal amplitude for all missions and modes. We also found that the  
 279 absolute magnitude of both the trend and amplitude increased linearly as the search radius increased. We interpret  
 280 this result as a decrease in efficiency of the correction, possibly due to de-correlation with increasing  
 281 spatial/temporal scales. The use of a 1 km search radius is also computationally efficient as less data are used in  
 282 the inversion. Applying these lessons to the ice sheet wide processing, we found that the correction has a minor  
 283 impact on the estimated trend for the CryoSat-2 SARIn-mode and the Geosat missions. We also found that the  
 284 application of the correction to the SARIn and Geosat data increased the seasonal amplitude of the local (single  
 285 grid cell) time series (Section 3.2.4). Given that there is no physical justification for an increase in seasonal  
 286 amplitude, we chose not to apply the correction to the Geosat mission and the SARIn-mode data. For the other  
 287 missions, the magnitude of the correction varied across missions and modes of operation, where the largest

288 changes in trend and amplitude were found for Envisat and ERS-2 ice mode, and the lowest for CryoSat-2 LRM.  
 289 By examining the changes in trend and amplitude we found significant spatial patterns, also varying across each  
 290 mission and mode, as shown in Figure 3. These patterns show strong correlations to both surface slope/roughness  
 291 and signals of metrological origin (Armitage et al., 2014) and are mostly driven by katabatic winds and the re-  
 292 distribution of snow. The wind effect can be observed in the RMSE plots for Envisat and for ERS-2 Ice as banned  
 293 structures East Antarctic sector following the main ridge lines.  
 294



295  
 296 Figure 3: Change in elevation change rate and RMSE (seasonal amplitude) of the local time series after correction  
 297 for temporal changes in scattering penetration depth). Spatial patterns linked to surface conditions can be clearly  
 298 observed. These effects are most prominent for Envisat and ERS-2.  
 299

### 300 3.2.3 Cross-calibration and integration

301 Removal of the time-invariant surface topography is done internally to each dataset such that elevation residuals  
 302 are not aligned to the same surface (see Section 3.2.1). To align elevation anomalies to a common reference we  
 303 first solve for inter-mission offsets. These offsets vary regionally (Khvorostovsky, 2012; Wingham et al., 2009;  
 304 Zwally et al., 2005), depending on the underlying topography, physical interactions of the radar with the surface,  
 305 and differing retracking methodologies. In contrast to previous studies (e.g., Davis, 2005; Khvorostovsky, 2012;  
 306 Li et al., 2006; Schröder et al., 2019; Wingham et al., 2006, 2009; Zwally et al., 2005), we estimate these offsets  
 307 using a least-squares adjustment. This approach allows for a simple, yet consistent, alignment of multiple relative  
 308 elevation anomalies without requiring full overlap between missions to solve. The technique follows the approach  
 309 of Bevis et al. (2014), using the entire multi-mission record to constrain the solution while accounting for trend,  
 310 seasonality and inter-mission/mode offsets. The trend is represented by a polynomial, with a maximum order of  
 311 six; a four-term Fourier series to account for seasonality; and Heaviside functions to solve for the inter-mission  
 312 offset between missions and modes. The design matrix can be written as:

$$h(t) = \sum_{i=1}^{n_p-1} p_i(t - t_r)^{i-1} + \sum_{k=1}^{n_f} s_k \sin\left(\frac{2\pi t}{T_k}\right) + c_k \cos\left(\frac{2\pi t}{T_k}\right) + \sum_{j=1}^{n_j} b_j h \quad (2)$$

313

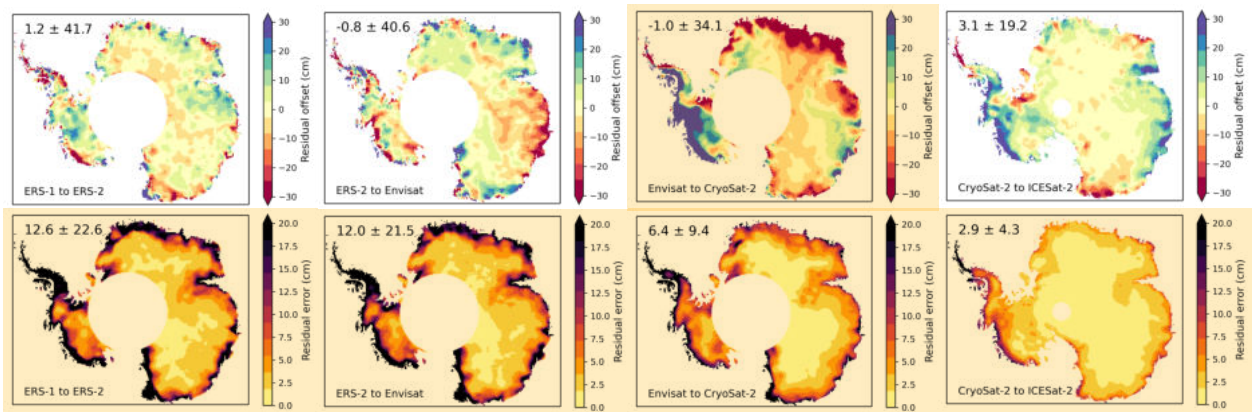
314 where  $n_p$  is the model order,  $t$  is the time in decimal years,  $t_r$  is the reference time in decimal years ( $t_r =$   
315 2013.95),  $T_k$  is the seasonal period reference ( $T_1 = 1$  and  $T_2 = 0.5$ ),  $n_f$  is the number of Fourier series terms ( $n_f =$   
316 4) and  $n_j$  is the number of missions and modes ( $n_j = 10$ ).

317  
318 Here, we add offsets for ten different missions and modes in the least squares model (Geosat, ERS-1 Ocean/Ice,  
319 ERS-2 Ocean/Ice, Envisat, ICESat, CryoSat-2 LRM/SARIn and ICESat-1) to all data falling within the search  
320 radius. To determine the order of the polynomial we use the Bayesian Information Criterion (BIC: Fabozzi et al.,  
321 2014; Schwarz, 1978) to select the polynomial that produces the lowest BIC-value estimated from monthly binned  
322 data.

323  
324 The cross-calibration is performed on a 2 km polar-stereographic grid (EPSG: 3031) using a variable search radius  
325 of 1-10 km surrounding each grid-cell. The radius is increased until 70% of the time series is filled (monthly) or  
326 the maximum radius is reached. If the maximum search radius is reached and the 70% criteria is not meet, we  
327 continue processing using all available data. In most cases the search radius is in the range of 2-10 km. Outliers  
328 in the original time series were initially removed using a 1-year running median filter where values larger than  
329 ten times the median absolute deviation (MAD) are rejected. The model is then fit to the time series using a robust  
330 least-squares inversion as in Sect. 3.2.1. Solutions are rejected if the absolute value<sup>\*</sup> of the linear rate is larger than  
331 20 m a<sup>-1</sup> or if the RMS of the time series relative to the model is larger than 4 m. If any of the derived offsets are  
332 larger than 100 m the offset is set to zero. The offsets estimated from the least-squares<sup>\*</sup> inversion are then subtracted  
333 from the time series providing an initial cross-calibrated record of elevation change. Further, a last outlier step is  
334 performed where the model is used to filter the time series by omitting observations exceeding ten-times<sup>\*</sup> the MAD  
335 of the model-residuals.

336  
337 This approach has several advantages; it allows a first order calibration of non-overlapping time series while also  
338 aligning overlapping missions and modes to their common mean. To account for time series that do not fully  
339 conform to our choice of a linear model, a secondary cross-calibration is performed for the four mission-specific  
340 offset coefficients (ERS-1 to ERS-2, ERS-2 to Envisat/ICESat, Envisat/ICESat to CryoSat-2 and CryoSat-2 to  
341 ICESat-2), using the post-fit model residuals. This approach was chosen as it facilitates the estimation of any  
342 residual offsets after removal of the majority of the trend and seasonality, making it simple to estimate the overall  
343 bias between the mission groups. The offsets for groups<sup>\*</sup> ERS-1 to ERS-2, ERS-2 to Envisat/ICESat and CryoSat-  
344 2 to ICESat-2 were estimated by taking the median<sup>\*</sup> difference between the two datasets over their respective  
345 overlapping time periods. This approach was found to be suboptimal for the Envisat/ICESat to CryoSat-2 offsets  
346 due to the short period of overlap (less than 4 month)<sup>\*</sup> and large changes during the time period 2009-2011. To  
347 overcome this limitation, we applied three different<sup>\*</sup> methods, generating five different independent  
348 Envisat/ICESat to CryoSat-2 offsets at each search node. Method<sup>\*</sup> 1: We fit two second order polynomials to the  
349 two residual time series and compute the median offset between<sup>\*</sup> the two functions over a one-year overlap (2010-  
350 2011), and the difference between the two intercepts of the<sup>\*</sup> polynomials. Method 2: We applied a Kalman  
351 Smoother with a state-space model consisting of a constant local<sup>\*</sup> level and a random-walk trend (Kalman, 1960;  
352 Shumway and Stoffer, 1982) that better accommodates the variability in the time series. The filter was initialized  
353 with a variance rate of 1 mm<sup>2</sup> a<sup>-3</sup> (Davis et al., 2012), with<sup>\*</sup> the observational noise given by the RMSE of each

354 residual time series. Initial state-values of the filter were set to zero for both the level and trend with large initial  
 355 uncertainties (1e6). The filter parameters were then optimized using the expectation-maximization (EM)  
 356 algorithm (Shumway and Stoffer, 1982) with five iterations. The same approach as in Method 1 was used to  
 357 generate the two estimates of the offset based on the one-year overlap, and the differencing of the two intercepts.  
 358 Method 3: Here the offsets were determined by computing the median difference between the two missions over  
 359 the 2010-2011 time period. To determine which of the offsets produces the best cross-calibration, we apply each  
 360 offset and compute linear rates of change from 2003 to 2019. These rates are then compared to rates estimated  
 361 from unbiased ICESat/ICESat-2 measurements produced by Smith et al., (2020), and the offset with the smallest  
 362 absolute difference was selected. Finally, the selected offsets rate difference (radar minus laser) is checked against  
 363 the difference computed without a residual cross-calibration. If the applied offset did not improve the rate  
 364 compared to the ICESat/ICESat-2 record, then the residual offset was set to zero. Following Schröder et al.,  
 365 (2019), we remove outliers in the offsets using a 100x100 km 5-MAD moving spatial filter. The intermission  
 366 offsets are then interpolated using a gaussian kernel with a 20 km correlation length using the nine closest data  
 367 points. This produces a spatially consistent field of offsets for the cross-calibration of the elevation residuals. Then  
 368 the offsets estimated from the initial least-squares adjustment, and the offsets estimated from the secondary  
 369 residual calibration are then applied to create a fully calibrated local time series. Finally, the individual calibrated  
 370 elevation time series for each mission/mode are averaged to monthly estimates of elevation change for each spatial  
 371 grid cell, with an associated standard error. Once, the time series have been calibrated a seasonal amplitude  
 372 correction is applied to the data to normalize amplitudes between missions. This is described in more detail in  
 373 Section 3.2.4. Finally, the monthly normalized time series are then combined and integrated into a continuous  
 374 record using the weighted average of the data within each overlapping temporal bin. Weights are specified as the  
 375 inverse variance of each mission's accuracy, and the random error estimated from the monthly averaging  
 376 procedure (see 4.1).  
 377



378  
 379 Figure 4. Maps of the residual cross-calibration offset and the corresponding error for the three main inter-mission  
 380 transition periods. One should note that here ICESat has been grouped with Envisat in the initial calibration.  
 381  
 382  
 383  
 384  
 385

386 The initial least-squares adjustment provided good alignment between overlapping modes (ocean/ice mode) and  
 387 missions (Envisat-ICESat), and a first order correction for the three weakly overlapping missions that allows for  
 388 better estimation of the residual biases from the detrended data. Initial offsets were determined to be as large as  
 389 10-15 m in areas of rapid change such as Pine Island Glacier. However, the least-squares adjustment was shown  
 390 to be inadequate when large non-linear elevation changes are present. The magnitude of the estimated residual  
 391 cross-calibration error (after least-squares adjustment) (Figure 4) show that most overlapping regions<sup>\*</sup> have a  
 392 clear correlation with temporal coincident elevation change rates. This pattern is evident in the Envisat to  
 393 CryoSat-2 transition (Figure 4) for Dronning Maud Land (Basins 5-8), Wilkes Land (Basins 12-13),  
 394 Bellingshausen Sea (Basins 23-25) and the Amundsen Sea sector (Basins 20-23) (Figure 10: 2010-2012). For  
 395 the ERS-2 to Envisat transition, we find a clear correlation between the<sup>\*</sup> magnitude of the offsets and the changes  
 396 in elevation due to variations in surface mass balance in Wilkes's land (Basins 12-13 seen in Figure 1), over the  
 397 2001-2003 time period (Schröder et al., 2019).

### 398 3.2.4 Normalization of seasonal amplitude

399 The radar signal's interaction with the surface and sub-surface firn-layers can create artificially large seasonal  
 400 amplitudes and trends, as described in Sect. 3.2.2. We correct for these as best possible using information  
 401 contained in the waveform parameters. However, in many cases these corrections are unable to fully correct the  
 402 artificial signals. This behavior can be seen in Schröder et al., (2019) and in our data, even after the scattering  
 403 correction has been applied there exists intermission variations in seasonal amplitude (Figure 5). To further reduce  
 404 this effect, we apply an amplitude correction ( $h_n$ ) to each mission to normalize the seasonal signal<sup>\*</sup> over the entire  
 405 record. We normalized the seasonal amplitudes of the ERS 1 & 2 and Envisat records to match amplitudes  
 406 computed from the CryoSat-2. CryoSat-2, which is retracked with a much lower threshold of the maximum  
 407 waveform amplitude (10%) for LRM and a maximum gradient threshold for SARin, has been shown<sup>\*</sup> to be less  
 408 sensitive to changes in surface properties and produces seasonal amplitudes of the same magnitude as ICESat  
 409 (Figure 5) (Nilsson et al., 2016). "After removal of the long-term trend, the amplitude normalization was computed  
 410 for each mission, except for<sup>\*</sup> ICESat and CryoSat-2, according to:

411

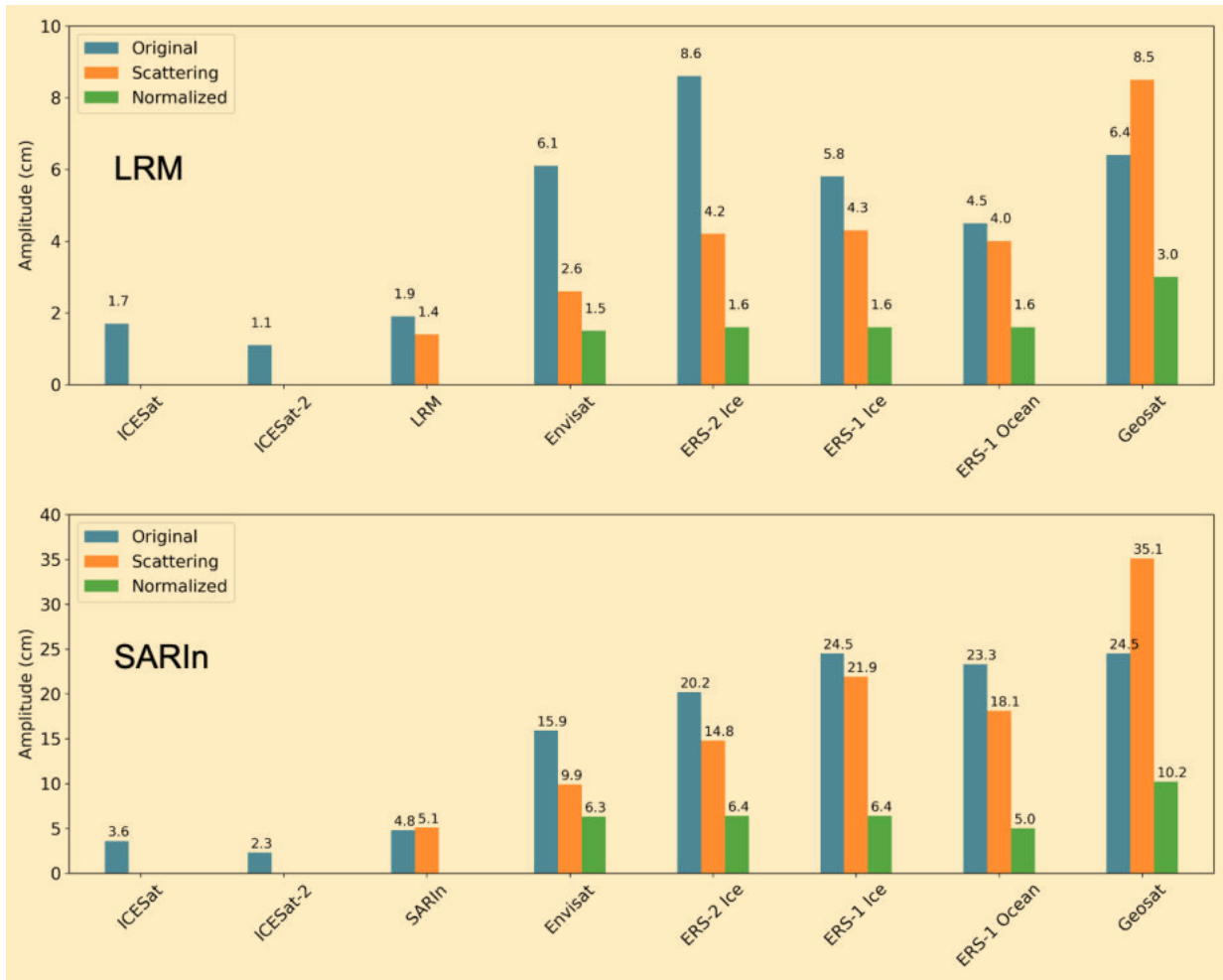
$$411 \quad h_i = \left(1 - \frac{a_i}{a_r}\right) \cdot [\alpha_c \cos(2\pi t) + \alpha_s \sin(2\pi t)] \quad (3)$$

412

413 where ( $a_i$ ) is the amplitude of the mission ( $a^2 = \alpha_c^2 + \alpha_s^2$ ), ( $a_r$ ) is the reference amplitude estimated from  
 414 CryoSat-2 data and  $\alpha_{c,s}^2$  are the coefficients for the seasonal model. The correction is applied by subtracting it  
 415 from each individual time series and the normalization<sup>\*</sup> has the effect of producing more homogeneous amplitudes  
 416 over the entire altimetry record. The application did<sup>\*</sup> not introduce any noticeable shift in the phase of the seasonal  
 417 signal.

418

419 ICESat and the CryoSat-2 LRM mode show similar magnitude in amplitude and supports the choice of using  
 420 CryoSat-2 as reference where the difference is most likely explained by the lower temporal sampling of ICESat.  
 421 The slightly lower seasonal amplitude of ICESat-2 is mostly likely due to the short time span used to estimate the  
 422 amplitude (2-years), as seen in Figure 5.



423  
 424 Figure 5. Top: Median seasonal amplitude of the different missions and modes for the CryoSat-2 LRM (top) and  
 425 SARin (bottom) mode masks (South of 81.5° S for LRM). The blue bars show the original seasonal amplitude  
 426 with no corrections applied, the orange bars show the amplitude once the mission dependent scattering correction  
 427 has been applied, and the green bars show the normalized amplitude after adjustment using CryoSat-2 as reference.

### 428 3.2.5 Interpolation, extrapolation and filtering

429 Collocation (a.k.a. ordinary kriging; Herzfeld, 1992; Nilsson et al., 2016) was used to interpolate the monthly  
 430 elevation change estimates onto a 1920 m grid using a maximum search radius of 50 km and a 20 km correlation  
 431 length. The 1920 m was chosen to be consistent with the ITS\_LIVE grid that accommodates nesting of datasets  
 432 at multiple resolutions. An adaptation to Nilsson et al. (2016) is that the local average is replaced by an estimate  
 433 from a linear model regressed against both surface elevation (bedmap2) and surface velocity from Gardner et al.  
 434 (2018), available at (<https://its-live.jpl.nasa.gov>), following the approach of Hurkmans et al. (2012) as seen below:  
 435

$$436 \quad m_0 = \beta_0 + \beta_1 h_{DEM} + \beta_2 \log(v) \quad (4)$$

437 where ( $h_{DEM}$ ) is elevation values from the DEM (bedmap2) and ( $v$ ) are the surface velocity values. The minimum  
 438 surface velocity is capped at 50 m per year to avoid introducing noise in the interior parts of the ice sheet and the  
 439 logarithm is applied to linearize the range of velocity values.

440 For the interpolation, the spatial variance is taken to be the mean of the random error estimated from the monthly  
441 averaging procedure. The noise term (diagonal of the error matrix), used in the collocation to weight each  
442 observation, is taken as root-sum-square (RSS) of the variance of the cross-calibration error, mission accuracy  
443 and the random error (see Section 4.1). Further, a minimum error of 5 cm is given to all observations based on  
444 ICESat and ICESat-2 crossover analysis (Section 5.1, Table 1). Prior to the interpolation we remove erroneous  
445 observations using a 100 km radius spatial filter centered at the location of each data value. In this procedure,  
446 following Smith et al. (2020), we remove spatial gradients inside each 100 km cap by fitting a biquadratic surface  
447 and if the observation exceeds a specific threshold it is removed. This threshold is dependent on the local surface  
448 roughness and elevation change rate, where the surface roughness is estimated from the bedmap2 DEM. If the  
449 surface roughness is larger than 60 m and the absolute elevation change rate is less than  $0.2 \text{ m a}^{-1}$  (Smith et al.  
450 2020), then the filter threshold is set to 3-MAD otherwise set to 30-MAD (gross-outliers). This has the effect that  
451 the filter is more aggressive in regions of steep topography (Antarctic Peninsula and the Transantarctic Mountains)  
452 while preserving signal in areas of rapid change. In the temporal domain, and after spatial interpolation, a 12-  
453 month median filter is applied to remove outliers exceeding the 10-MAD threshold. Rejected values in the time  
454 series are filled using a gaussian kernel with a correlation length of 3-months.

455  
456 Differences in satellite orbits cause spatial coverage to vary from  $81.5^\circ - 88^\circ \text{ S}$  (excluding Geosat that only reached  
457  $72^\circ \text{ S}$ ). The large gap in coverage between the maximum latitude reached and the south pole is referred to as the  
458 pole hole. To create a spatially complete record of elevation change we use extrapolation to fill the pole hole for  
459 each monthly time epoch. We first average each monthly spatial field to a coarse 20 km resolution, corresponding  
460 to the average correlation length of the elevation anomalies. We then fill the CryoSat-2 and ICESat-2 pole holes  
461 using our collocation/kriging algorithm (with velocity and elevation terms set to zero), similar to Zwally et al.  
462 (2015), using the 200 closest 20 km averaged values, with a correlation length of 100 km, and provide each  
463 averaged observation with the aggregated error within each cell. For the  $81.5^\circ \text{ S}$  missions (ERS 1/2 and Envisat)  
464 the unobserved area is about eighteen times larger than the area for CryoSat-2 and ICESat-2. This makes our  
465 extrapolation approaches less useful. To overcome this issue, we remove a linear trend and the annual seasonal  
466 signal estimated over the ICESat, CryoSat-2 and ICESat-2 period for each grid-cell over the 1992-2020 period.  
467 The residuals to this model are more homogeneous in the far field. We then extrapolate these residuals to the  
468 entirety of the  $81.5^\circ$  pole hole for each month using the same spatial kriging/collocation algorithm as previous  
469 used (velocity and elevation set to zero). After the monthly residuals have been gridded and filled, we add back  
470 the linear trend and seasonality estimated from the CryoSat-2 and ICESat/2 model for each location. For both  
471 approaches we multiply the predicted errors from the algorithm with a factor of three to avoid errors that are too  
472 small (e.g., less than 5 cm as estimated from ICESat-2 as in Table 1.). The estimated errors for the pole-hole are  
473 to be considered only as a guide. These errors are based on the error-statistics of the surrounding 20 km averaged  
474 data and errors being extrapolated inward to the pole, such as data from the Transantarctic mountains. This can  
475 provide a somewhat unrealistic looking spatial pattern for the estimated error field, but which is still based on  
476 observations.

477  
478 Interpolated elevation anomalies can easily be included or excluded in any future analysis using the *data\_flag*  
479 field that is included with the data product: 0 = no data, 1 = high quality data, 2 = low quality data, 3 = pole hole.



480 The “low<sup>\*</sup> quality data” index is based on a minimum bedmap2 surface roughness criteria that is set to the  
481 approximate size of the range gate window of the radar altimeters (roughness threshold for Geosat: 30 m, ERS-  
482 1/2 and Envisat: 120 m, and CryoSat-2: 240 m). We also provided the ESA COP DEM  
483 (<https://spacedata.copernicus.eu/web/cscda/dataset-details?articleId=394198>) resampled to our 1920 m grid using  
484 a box-filter (averaging) to allow the user to investigate time-evolving topography. Center date of the DEM is circa  
485 2010-2015 which is in line with our provided center or reference date of 2013-12-16.

486  
487 To estimate volume changes at the basin scale (Figure 1), we replaced the interpolated values flagged by the  
488 surface roughness criterion with values estimated from a hypsometric relationship (Moholdt et al., 2010; Nilsson  
489 et al., 2015b). Here, the monthly values of elevation change (excluding the values flagged by roughness) were  
490 binned using the median value within 100 m elevation intervals according to the hypsometry provided by the  
491 DEM (bedmap2). As in Morris et al. (2020), a linear model was fit to these binned values and used to extrapolate  
492 values to areas<sup>\*</sup> flagged as “low quality data”. This was done only for the purpose of this paper and is not applied  
493 to the final data product. This choice was made to allow the users to select a suitable method given their interest  
494 or constraints.

## 495 4 Error propagation and validation

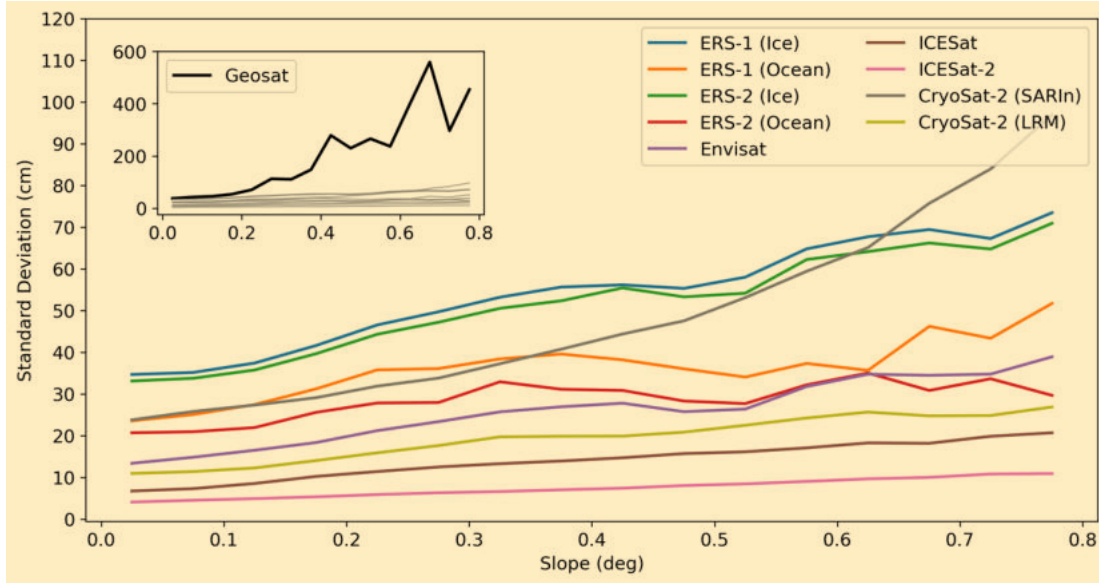
### 496 4.1 Uncertainties of elevation change time series and data

497 An internal crossover analysis was performed to determine the relative accuracy of each mission and mode in a  
498 similar manner as Brenner et al. (2007) and Schröder et al. (2019). We estimated the standard deviation of all  
499 crossovers with a time difference of less than 31-days. Crossovers were binned as a function of surface slope at  
500 intervals of 0.04° (Figure 6). The relative accuracy of each mission or mode was determined from the standard  
501 deviation at zero slope by fitting an error function (inside an interval of 0 - 0.4°) as shown in Table 1. To derive  
502 the uncertainty of each time series epoch we use the spatiotemporal variability inside each monthly time interval,  
503 in the form of the standard deviation. This provides a random error for each monthly value that varies both in  
504 space and in time and encompasses measurement related errors driven by topography, retracking and range  
505 corrections etc. To quantify the total cross-calibration error for each time series we use the standard deviation of  
506 each grouped mission offsets (Section 3.2.3) and add them in quadrature to estimate the total cross-calibration  
507 error, similar to Schröder et al. (2019). We then have the total error ( $\sigma_m$ ) for<sup>\*</sup> each month in each time series by  
508 summing the individual error sources as:

$$\sigma_m^2 = \sigma_i^2 + \sigma_c^2 \quad (5)$$

509  
510 where ( $\sigma_m$ ) the error due to the elevation change variability within each monthly interval for each time series and  
511 ( $\sigma_c$ ) is the total cross-calibration error for each time series. The estimated total error ( $\sigma_m^2$ ) is the provided RMS-  
512 error in the product (varying both by location and time).

513



514  
 515 Figure 6. Standard deviation (cm) of intra-mission and intra-mode crossovers for the Antarctic Ice Sheet as a  
 516 function of surface slope (degrees). Precision decreases quasi-linearly as surface slope increases.

517  
 518 Table 1. Sensor and mode errors ( $\sigma_{mission}$ ) as a function of the random ( $\sigma_{noise}$ ) and slope dependent ( $\sigma_{slope}$ )  
 519 errors. Slope ( $\alpha$ ) is in degrees. Modelled error ( $\sigma_{mission}$ ) is based on fitting the following function to the intra-  
 520 sensor, intra-mode crossover data:  $\sigma_{mission} = \sigma_{noise} + \sigma_{slope}\alpha^2$

Mission	$\sigma_{noise}$ (cm)	$\sigma_{slope}$ (cm)
Geosat	36	793
ERS-1 (Ice)	36	159
ERS-1 (Ocean)	26	114
ERS-2 (Ice)	34	147
ERS-2 (Ocean)	22	89
Envisat	15	97
ICESat	8	51
ICESat-2	5	20
CryoSat-2 (SARIn)	25	115
CryoSat-2 (LRM)	12	70

534 **4.2 Validation of rates of elevation change**

535 To validate the data product, we computed elevation change rates and compared them to rates derived from near-  
 536 coincident Operation IceBridge (OIB: MacGregor et al. (2021)) and pre-OIB data spanning the period 2002 to  
 537 2019 using the Airborne Topographic Mapper (ATM: MacGregor et al. (2021)) laser altimeter. Elevation change  
 538 rates for ATM were derived following the approach of Nilsson et al. (2016), where a linear model was solved at  
 539 each measurement location using a search radius of 175 m. Following the approach of McMillan et al. (2014) and  
 540 Wouters et al. (2015), the local slope was used to correct the measurements to the reference track, indicated as

541 Track\_Identifier = 0 in the product. Solutions were rejected if they contained less than two campaigns of ATM  
 542 data, the magnitude of linear rate was larger than  $10 \text{ m a}^{-1}$ , the standard deviation of the solution exceeded  $1 \text{ m a}^{-1}$ ,  
 543 or if the solution contained less than 10 measurements, and if the time span was less than two years. The  
 544 elevation accuracy of the ATM sensor family has an estimated error of less than 9 cm (Brunt et al., 2017),  
 545 corresponding to an accuracy of roughly  $0.5 \text{ cm a}^{-1}$  over the 18-year measurement period. Operation IceBridge  
 546 coverage is concentrated to the western parts of the Antarctic Ice Sheet, providing very limited coverage in the  
 547 East. To overcome this limitation, we also use elevation change rates estimated by Smith et al. (2020) that are  
 548 based on crossover analyses of satellite laser altimetry (ICESat and ICESat-2: 2003-2019) that has an error of  
 549 roughly 10 cm. This corresponds to an error in the rate of elevation change of about  $0.6 \text{ cm a}^{-1}$ , which is consistent  
 550 with the error observed for ATM. These errors and their impact are discussed further in Section 5.

551

### 552 4.3. Area integrated error estimation

553 Area integrated error for each drainage region, based on the outlines from Zwally et al. (2012) (shown in Figure  
 554 1), are estimated loosely following the approach of Nilsson et al. (2016). The total area integrated error is divided  
 555 into three main components: the systematic bias, the random error and the rate error estimated in the fitting  
 556 procedure. These are then combined in quadrature to produce the total error according to:

557

$$\sigma_{tot}^2 = \sigma_s^2 + \frac{\sigma_r^2}{n} + \frac{\sigma_h^2}{n-k} \quad (6)$$

558

559 where  $\sigma_s$  is the systematic bias,  $\sigma_r$  the random error,  $\sigma_h$  the rate error,  $n$  is the number of uncorrelated elevation  
 560 change estimates (see below) and  $k$  is the degrees of freedom in the least squares model ( $k = 2$ ). The systematic  
 561 bias and the random error are taken as the average and standard deviation of the difference in rate between the  
 562 JPL (this study) and ICESat-ICESat-2 (Smith et al. 2020) products for the 2003-2019 period. We compute the  
 563 error in the estimated rate using the variance-covariance matrix in the least square fitting procedure according to:

564

$$\sigma_h^2 = \bar{\sigma}_m^2 \cdot \text{diag}[(X^T X)^{-1}]_h \quad (7)$$

565

566 where  $\bar{\sigma}_m$  is the average monthly uncertainty from our product inside the time interval of interest,  $X$  is the design  
 567 matrix of the linear model,  $X^T$  is the transpose of the design matrix,  $\text{diag}$  the diagonal elements of the array and  
 568  $()^{-1}$  the inverse of the dot products. The subscript  $h$  is the location of the rate error in the diagonal array. To  
 569 account for spatial autocorrelation  $\sigma_r$  and  $\sigma_h$  are divided by  $n$ .  $n$  is estimated by dividing the total area of each  
 570 drainage region with the correlation area:  $n = A/\pi\rho^2$  where  $A$  is the area of the region and  $\rho$  is the correlation  
 571 length. The errors for each drainage region are summarized in Table 2. The intrinsic quality of each mission was  
 572 determined through internal crossover analysis (Section 4.1) of each mode and mission and is summarized in  
 573 Table 1 and Fig. 6. Analyzing the correlation length of the laser-only versus JPL elevation change differences we  
 574 find an ice sheet wide correlation length-scale on the order of 20-100 km. To be conservative, a correlation length  
 575 of 100 km was used to compute  $n$ .

576

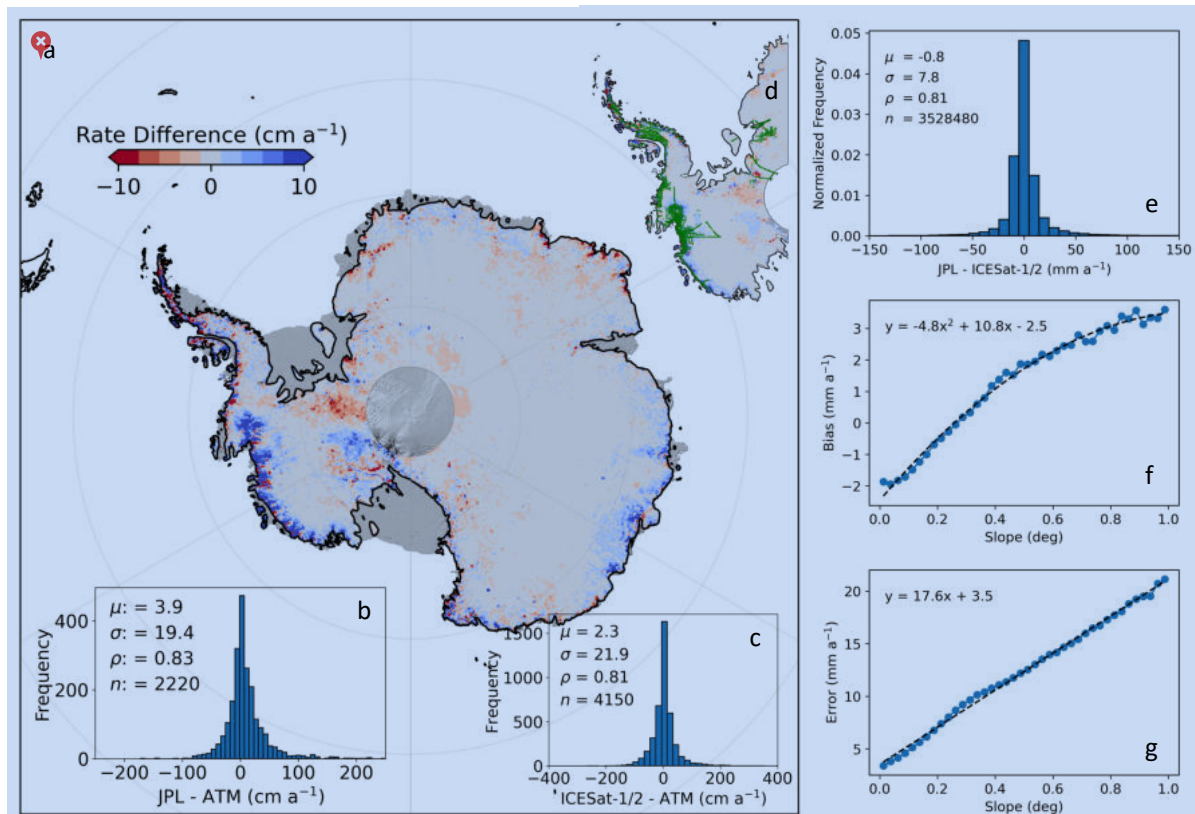
577 Table 2. Regionally averaged errors for the synthesized JPL record of elevation change, computed relative to the  
578 unbiased ICESat to ICESat-2 estimate of Smith et al (2020). Errors were determined by differencing 2003-2019  
579 linear rates of elevation change between products. The bias (mean) and error (standard deviation) are computed  
580 for each drainage basin (1-27: Figure 1). Antarctic Ice Sheet (AIS), Antarctic Peninsula (AP), West Antarctic Ice  
581 Sheet (WAIS) and East Antarctic Ice Sheet (EAIS) statistics are determined using area weighted averages.  
582

Region	Bias (mm a <sup>-1</sup> )	Error (mm a <sup>-1</sup> )	Area (km <sup>2</sup> )	Corr. length (km)
1	-4.1	16.0	510200	112
2	-9.1	12.6	754800	62
3	-2.3	4.7	1516300	46
4	-2.4	11.0	267300	28
5	2.4	9.2	199700	47
6	-1.2	9.4	633900	39
7	-6.9	7.8	526000	20
8	-1.8	9.6	176900	21
9	2.5	7.6	161100	27
10	-2.9	4.4	890600	14
11	0.3	4.1	262300	10
12	3.9	6.6	754700	50
13	2.7	5.6	1142500	64
14	-1.4	5.5	742500	11
15	6.8	27.5	150300	9
16	-2.2	6.8	269800	23
17	-2.2	5.2	1795600	59
18	3.5	21.3	270600	29
19	2.3	6.3	373700	30
20	26.4	34.6	217300	20
21	8.9	16.3	224500	51
22	11.0	24.4	215700	71
23	-1.0	29.1	101400	13
24	-0.4	26.7	118000	14
25	-0.3	147.8	61500	13
26	-8.3	78.2	74600	8
27	0.1	28.1	68700	12
EAIS	-1.55	6.85	7653900	41
AP	-2.1	61.97	233300	12
WAIS	5.08	18.64	1453200	57
AIS	-0.55	10.08	9340400	43

## 583 **5 Results**

### 584 **5.1 Accuracy of synthesis**

585 Previous studies have relied on near co-incident airborne measurements to validate land ice elevation changes  
586 derived from multi-mission synthesis (McMillan et al., 2014; Nilsson et al., 2016; Simonsen and Sørensen, 2017;  
587 Wouters et al., 2015). This approach, however, is limited in both the spatial and temporal coverage. For Antarctica,  
588 airborne validation data has been collected during austral summer, mostly over rapidly thinning glaciers, such as  
589 Pine Island and Thwaites, in the Western part of the ice sheet, with significant spatial coverage starting in 2002.  
590 The derived errors from these local comparisons are then extrapolated to the entire ice sheet, into regions  
591 exhibiting very different surface and metrological conditions. With the launch of ICESat-2 in September 2018 we  
592 now have, for the first time, the ability to compare long-term unbiased laser derived rates of elevation change on  
593 a continental scale. For this analysis we compare our synthesized rates of elevation change to those estimated by  
594 Smith et al. (2020) for the period 2003-2019 for each basin (Zwally et al., 2012) (Figure 1). The results of this  
595 analysis are summarized in Table 2. We find an ice sheet wide error of  $-0.8 \pm 7.8$  mm a<sup>-1</sup> (Figure 7e) with a  
596 quadratic and linear increase as a function of surface slope in the systematic bias and random error, respectively  
597 (Figure 7f-g). To determine the validity of this comparison we also compared ICESat-2 rates with rates from  
598 ATM over the time period 2003-2018. Good agreement was found between the two datasets with an average  
599 difference  $2.3 \pm 22$  cm a<sup>-1</sup> (Figure 7c) over regions with an observed rate of elevation change from ATM ranging  
600 from -15 to 2 m a<sup>-1</sup>. The main discrepancies between our product and the ICESat-2 derived elevation change  
601 are concentrated over areas of high-relief and over regions with large magnitude changes, such as Pine Island and  
602 Thwaites glaciers (Figure 7a). Here, differences larger than 10 cm a<sup>-1</sup> can be found, and for the main trunk of Pine  
603 Island glacier we find a difference of  $2 \pm 10$  cm a<sup>-1</sup> (Figure 7a). The magnitude of the ATM error compared to  
604 ICESat-2 product is larger. This is mostly due to the fact that the data comparison locations are in areas of rapid  
605 change. The correlation between the two laser datasets and our product is greater than 0.8 in both cases.



606  
 607 Figure 7. Elevation change validation and comparison using rates derived from ICESat - ICESat-2 and airborne  
 608 ATM data over the time period of 2003-2019 and 2001-2019, respectively. (a) shows the spatial distribution of  
 609 the elevation change differences from this study (JPL) differenced with rates derived from Smith et al. (2020). (b)  
 610 shows the comparison of rates derived from JPL with ATM at locations indicated in (d) with green flight lines.  
 611 (c) shows the comparison between ICESat - ICESat-2 derived rates with ATM. (e) depicts the ice sheet wide  
 612 histogram of elevation change differences. (b,c,e) include the distribution mean ( $\mu$ ), standard deviation ( $\sigma$ ),  
 613 correlation ( $\rho$ ), and number of observations ( $n$ ). (f-g) the bias (mean) and error (standard deviation) as a function  
 614 of surface slope for the JPL - ICESAT-1/2 validation.

615  
 616 The relative precision of the different satellite altimeters used in this study range from 5-40 cm over low slope  
 617 surfaces (Table 1 and Figure 6). Earlier missions such as Geosat, ERS-1 and ERS-2 are roughly three times less  
 618 precise than later missions (Envisat, ICESat/2 and CryoSat-2). However, it was also found that the ERS-1/2 ocean  
 619 mode was ~30% more precise than ice mode data, bringing it closely in line with the later missions. Unfortunately,  
 620 the data coverage of the ocean mode is far lower than the ice mode. For CryoSat-2, the lower relative precision  
 621 of the SARIn mode can be attributed to the spatial coverage, with SARIn operating over rougher terrain compared  
 622 to the LRM mode that operates over the interior of the ice sheet with a higher along-track resolution (i.e., smaller  
 623 footprint). Similar effects were also seen in Schröder et al. (2019). The laser altimetry missions show the lowest  
 624 noise levels, on the order of 5 cm over flat areas ranging up to 20 cm for slopes  $< 0.8^\circ$ , with ICESat-2 showing a  
 625 factor-of-two improvement in precision over its predecessor (ICESat) over all surface slopes.

## 626 5.7 Comparison to other studies and datasets

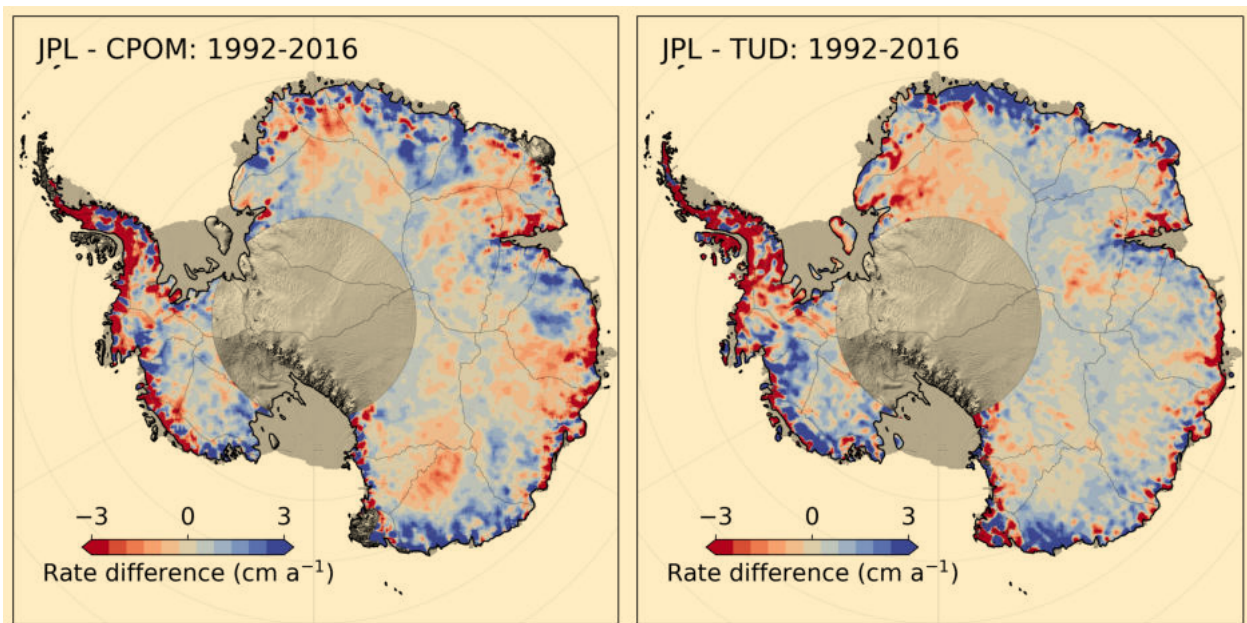
627 Previous long-term Antarctic Ice Sheet elevation change products have been produced by Dresden University of  
628 Technology (Schröder et al., 2019: TUD) and the Centre for Polar Observation & Modelling (Shepherd et al.,  
629 2019: CPOM). These products vary in both resolution and processing methodologies. The TUD product is  
630 provided at a spatial resolution of 10 km and as monthly elevation change estimates. In contrast, the CPOM  
631 product provides elevation change estimates every 5-years at 5 km resolution and basin wide time series of mass  
632 change at quarterly resolution. The TUD dataset is comprised of Seasat, Geosat, ERS-1/2, Envisat and CryoSat-  
633 2, while CPOM consists of data from ERS-1/2, Envisat and CryoSat-2. To allow for a fair comparison between  
634 the different products we used our provided product without hypsometric extrapolation for the analysis.

635  
636 The errors reported for our elevation change synthesis are slightly larger than those reported by TUD; this is due  
637 to the difference in retracking and the fitting procedure used to derive the error estimates. Comparing all three  
638 data products to the ATM validation data we find the best agreement with the JPL synthesis. (JPL:  $4 \pm 19$  cm a<sup>-1</sup>,  
639 TUD:  $6 \pm 20$  and CPOM:  $+4 \pm 53$  to  $-16 \pm 61$  cm a<sup>-1</sup>). The JPL and TUD estimates were computed from the same  
640 ATM dataset and given the same editing criteria, while values from CPOM are the reported values from Shepherd  
641 et al. (2019). Applying the same analysis to the 2007-2011 and 2011-2016 elevation change solutions provided  
642 by CPOM, we found values of  $29 \pm 41$  cm a<sup>-1</sup> (2007-2011) and  $-8 \pm 30$  cm a<sup>-1</sup> (2011-2016) for the comparison  
643 with ATM, and a weighted average of  $-2.2 \pm 33$  cm a<sup>-1</sup> comparing data from overlapping locations. To further  
644 compare the noise level in the different datasets we use the elevation change from the common 1992-2016 time  
645 period (as CPOM only provides rates in five-year intervals) of all products and compare against ICESat-ICESat-  
646 2 elevation change rate from 2003-2019. To reduce the impact of difference in time span, we initially compare  
647 only to data between 81.5° and 90° S (pole hole), as this spatial domain only contains ICESat and CryoSat-2  
648 measurements and is thus the most closely aligned in time with the ICESat-ICESat-2 estimate. We also perform  
649 an ice sheet wide analysis, though the time spans are not identical. To compute the noise level, we simply  
650 difference the three rate fields with the ICESat-ICESat-2 derived rates and computed the average and standard  
651 deviation of the differences. This provided the following ice sheet wide results:  $-0.32 \pm 1.70$  (JPL),  $-0.45 \pm 1.92$   
652 (TUD) and  $-0.33 \pm 2.59$  (CPOM) cm a<sup>-1</sup>. For the pole-hole region, 81.5° and 86° S, the following results were  
653 obtained:  $-0.33 \pm 1.17$  (JPL),  $-1.37 \pm 1.57$  (TUD) and  $-1.90 \pm 3.15$  (CPOM).

654  
655 Comparing the long-term rates for the overlapping time period 1992-2016, we find an overall good agreement for  
656 the three original products. Comparing only values North of 81.5° S, we determine volume change rates of -58, -  
657 48 and -59 km<sup>3</sup> a<sup>-1</sup> for JPL, TUD and CPOM, respectively. Differences are well within the errors for all the three  
658 products. Studying the differences in spatial patterns (Figure 8), using the JPL derived rate as the reference, we  
659 find that the TUD and JPL products agree well over East Antarctica in Basins 10-17 while a larger difference can  
660 be seen in Basin 3 closer to the Weddell Sea. Larger differences between JPL and CPOM compared to JPL versus  
661 TUD can be observed in East Antarctica (EAIS). This is likely a result of different methodologies for correcting  
662 changes in the radar scattering. Dividing the estimates into different regions we find the following volume change  
663 estimates for the 1992-2017 period: WAIS (JPL: -108, TUD: -100 and CPOM: -106 km<sup>3</sup> a<sup>-1</sup>), EAIS (JPL: 61,  
664 TUD: 48 and CPOM: 43 km<sup>3</sup> a<sup>-1</sup>) and AP (JPL: -11, TUD: 4 and CPOM: 5 km<sup>3</sup> a<sup>-1</sup>). The regional estimates agree

665 well among products, with the largest discrepancies found in the Antarctic Peninsula. Here, both the TUD and  
 666 CPOM products provide a positive volume change compared to the JPL-product, highlighting the challenge in  
 667 obtaining accurate estimates from this region. Comparing the JPL and TUD products with rates from Smith et al.  
 668 (2020) (ICESat/-2) over the time period 2003-2017 (again using the original JPL product with no hypsometric  
 669 extrapolation) we find that the two products agree well over WAIS (JPL: -165, TUD: -164, LA: -200 km<sup>3</sup> a<sup>-1</sup>), but  
 670 lower in magnitude compared to ICESat/-2 due to the larger radar footprint. For EAIS (JPL: 83, TUD: 51, LA:  
 671 85 km<sup>3</sup> a<sup>-1</sup>) a disagreement of roughly 40% is observed between the TUD and JPL products, where LA and JPL  
 672 values are practically identical. In the AP (JPL: -19, TUD: -7, LA: -39 km<sup>3</sup> a<sup>-1</sup>) both products are lower in  
 673 magnitude compared to ICESat/-2, on the order of 50-80% due to limitations in measuring over high relief  
 674 topography.

675

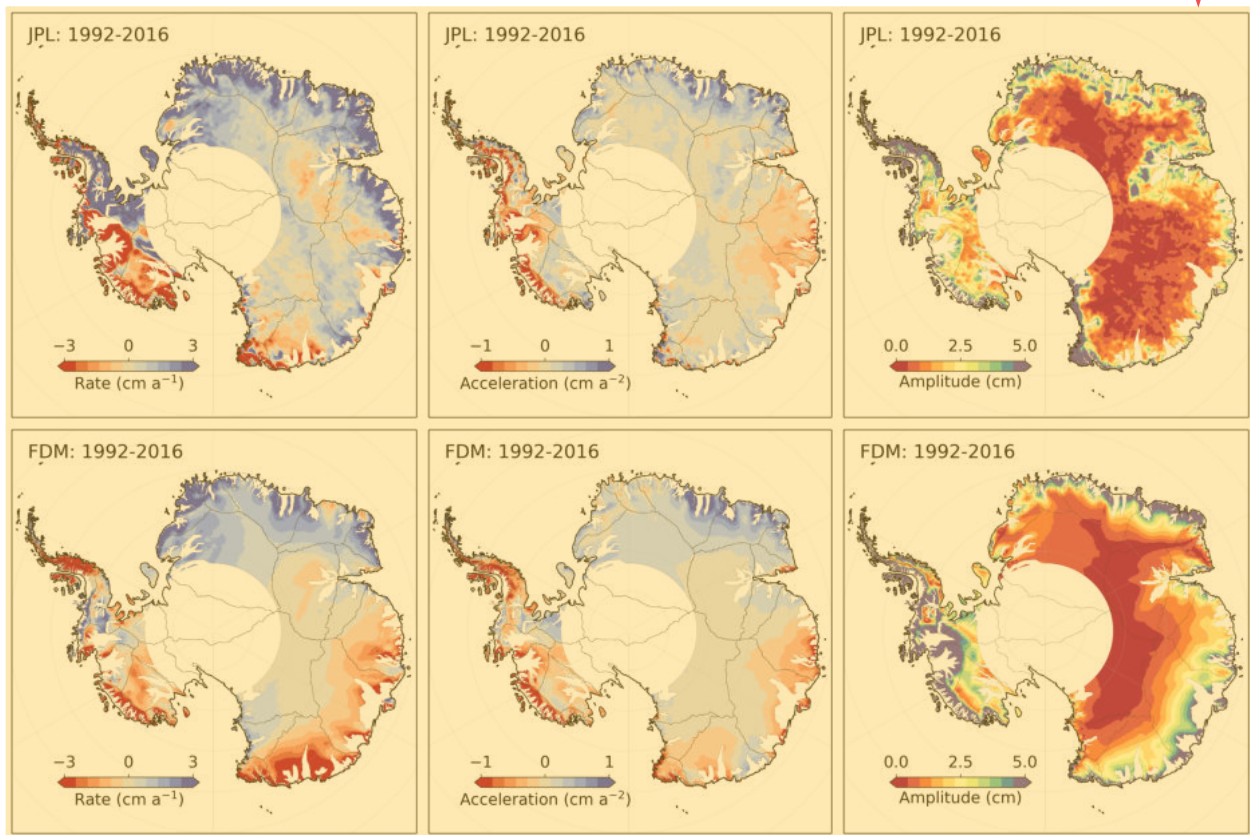


676  
 677 Figure 8: Comparison of overlapping long-term rates from the Technical University of Dresden (TUD) and Center  
 678 for Polar Observation and Modelling (CPOM) altimetry product with rates from this study (JPL).

679  
 680 To understand how well these products can capture (and provide insight into) the change/variability of physical  
 681 processes of the ice sheets, we compared our result with modeled changes in surface elevations (“zs”) from the  
 682 IMAU firm densification model (FDM: Ligtenberg et al. (2012)) that is forced by 6 hour mass balance components  
 683 (snowfall, rain, sublimation and snowmelt), average surface temperature, and 10 m windspeed, from the Regional  
 684 Atmospheric Climate Model, version 2.3p2 (van Wessem et al., 2018). The firm model only simulates changes in  
 685 surface elevation due to changes in surface processes and does not account for thinning or thickening resulting  
 686 from changes in ice dynamics (flow). To minimize dynamic signals, we mask areas with surface velocities larger  
 687 than 30 m a<sup>-1</sup> using the velocity field provided by the ITS\_LIVE project (Gardner et al., 2018) merged with Phase-  
 688 Based estimates (Mouginot et al., 2019). The surface elevation long-term trend and acceleration fields (1992-  
 689 2016), seen in Fig. 9, show that for Dronning Maud Land and Enderby Land (Basins 4-11) there is generally good  
 690 agreement in both the spatial pattern and the sign of the observed and modelled rate of elevation change. For these  
 691 regions, the observed change can be attributed to an increase in accumulation (Boening et al., 2012). However,



692 the magnitude between the modelled and measured rates of change differs by roughly 50%. The altimetry derived  
 693 volume change for basins 4-11, over the time period 1992-2016, is estimated at  $46 \text{ km}^3 \text{ a}^{-1}$  compared to a modelled  
 694 change of  $27 \text{ km}^3 \text{ a}^{-1}$ . This disagreement becomes even more prominent for Wilkes Land (basins 12-14) where the  
 695 difference between modelled and observed rates of change are larger and of opposite signs (Figure 9). For these  
 696 three basins, the estimated difference in volume change is on the order of  $36 \text{ km}^3 \text{ a}^{-1}$  based on the difference in the  
 697 modelled change of  $-25 \text{ km}^3 \text{ a}^{-1}$  compared to  $11 \text{ km}^3 \text{ a}^{-1}$  from altimetry. The magnitude and sign of these results  
 698 are consistent within all three altimetry products compared to the FDM. Further, comparing the differences in the  
 699 magnitude of the seasonal amplitude for 1992-2016, we find that the TUD product has an annual amplitude that  
 700 is ~50% larger than the JPL product ( $5.1 \pm 15$  versus  $2.7 \pm 4.9 \text{ cm}$ ). Our estimated value of  $2.7 \pm 4.9 \text{ cm}$  compares  
 701 well with the  $2.9 \pm 4.1 \text{ cm}$  average FDM amplitude for the period 1992-2016. This analysis was not applied to the  
 702 CPOM product as their provided basin time series are in units of mass, after a firm correction has been applied.



703  
 704 Figure 9: Spatial fields of rates (left column), acceleration (middle column) and seasonal amplitudes (right  
 705 column) from our product (JPL: top row) and modelled values from the IMAU firm densification model (FDM:  
 706 bottom row). Areas of fast flow ( $>30 \text{ m a}^{-1}$ ) have been masked out to minimize height changes caused by changes  
 707 in ice flow. The altimetry data has been smoothed with a 50 km median filter to highlight large scale spatial  
 708 patterns.

709  
 710  
 711

## 712 5.8 Basin-scale time-evolving volume change

713 Analyzing the 1992-2020 record of surface elevation (Table 3 and Figure 10-11), including the area between 81.5°  
714 and 90° S, we determine an average rate of volume change of  $-68 \pm 11 \text{ km}^3 \text{ a}^{-1}$  over the entire ice sheet, with large  
715 losses from the West Antarctic Ice sheet (WAIS:  $-113 \pm 6 \text{ km}^3 \text{ a}^{-1}$ ), and gains for East Antarctic Ice Sheet (EAIS:  
716  $+75 \pm 5 \text{ km}^3 \text{ a}^{-1}$ ) which experienced large snow-fall events in 2009 and 2011 (Boening et al., 2012). The Antarctic  
717 Peninsula (AP) is the most challenging region to measure elevation change, due to its extreme surface relief and  
718 sparse data coverage. We anticipate that any estimate derived from conventional satellite radar altimetry will be  
719 biased positive due to the inability to measure low elevation signals. That said, we estimate an overall negative  
720 trend for the AP of  $-27 \pm 8 \text{ km}^3 \text{ a}^{-1}$  for the 29-year record (1992-2020) (Figure 10-11) that align closely with other  
721 estimates (Groh et al., 2021; Rignot et al., 2019; Shepherd et al., 2018; Zwally et al., 2021), but is highly dependent  
722 on the applied hypsometric extrapolation (Section 3.2.5). On decadal time scales we find that the large glaciers  
723 systems of Pine Island, Thwaites, Smith and Kohler (Basins 21 and 22) show relatively stable mass loss since the  
724 early parts of the satellite era, with signs of accelerated thinning since 2007-2009 (Figure 11). WAIS has seen  
725 almost a doubling of its mass loss in the last decade (2011-2020) compared to the two previous decades (Figure  
726 11). EAIS has reverted back to its previous long-term decadal rate of  $\sim +8 \text{ km}^3 \text{ a}^{-1}$ , in line with the observed 5-  
727 year trend from Geosat over Dronning Maud Land (Figure 11,12), down from  $+84 \text{ km}^3 \text{ a}^{-1}$  following the anomalous  
728 snow-fall during the 2001-2011 period. AP was in balance and saw little observable change in the first decade  
729 (1991-2010), but increased its mass-loss by a factor of ten in the period of 2001-2011. The mass loss in the last  
730 decade was slowed by roughly 50% due to a positive mass balance anomaly during the period 2016-2018. Over  
731 the Geosat time period from 1985 to 1989, and for latitudes  $< 72^\circ \text{ S}$ , a general stable and small positive rate of  $6$   
732  $\pm 16 \text{ km}^3 \text{ a}^{-1}$  was found for the EA1 region (Basins 4-11, Figure 12). This rate remained stable between 1985 and  
733 2009 ( $\sim 10 \text{ km}^3 \text{ a}^{-1}$ ) until the onset of a precipitation event in 2009. For the EA2 region (Basins 12-15, Figure 1) a  
734 shift in both sign and magnitude was observed for the 1985-1989 period compared to the long-term positive rate  
735 for EA1. The mass loss over the 1985-1989 period was  $-70 \pm 22 \text{ km}^3 \text{ a}^{-1}$ , and found to be mostly driven by the  
736 Totten glacier system in Basin 13 (Figure 10). This rate is based, however, on heavy extrapolation over the Totten  
737 region, due to poor data coverage for the last two years of the mission, and should be treated with caution. Trends  
738 for EA2 showed a stable negative rate ( $\sim -25$ - $30 \text{ km}^3 \text{ a}^{-1}$ ) until 2001-2003 when a large positive change occurred  
739 due to an increase in SMB (Figure 10c). The region reverted back to long-term negative trend after 2006 mostly  
740 modulated by changes in SMB.

741

742

743

744

745

746

747

748

749

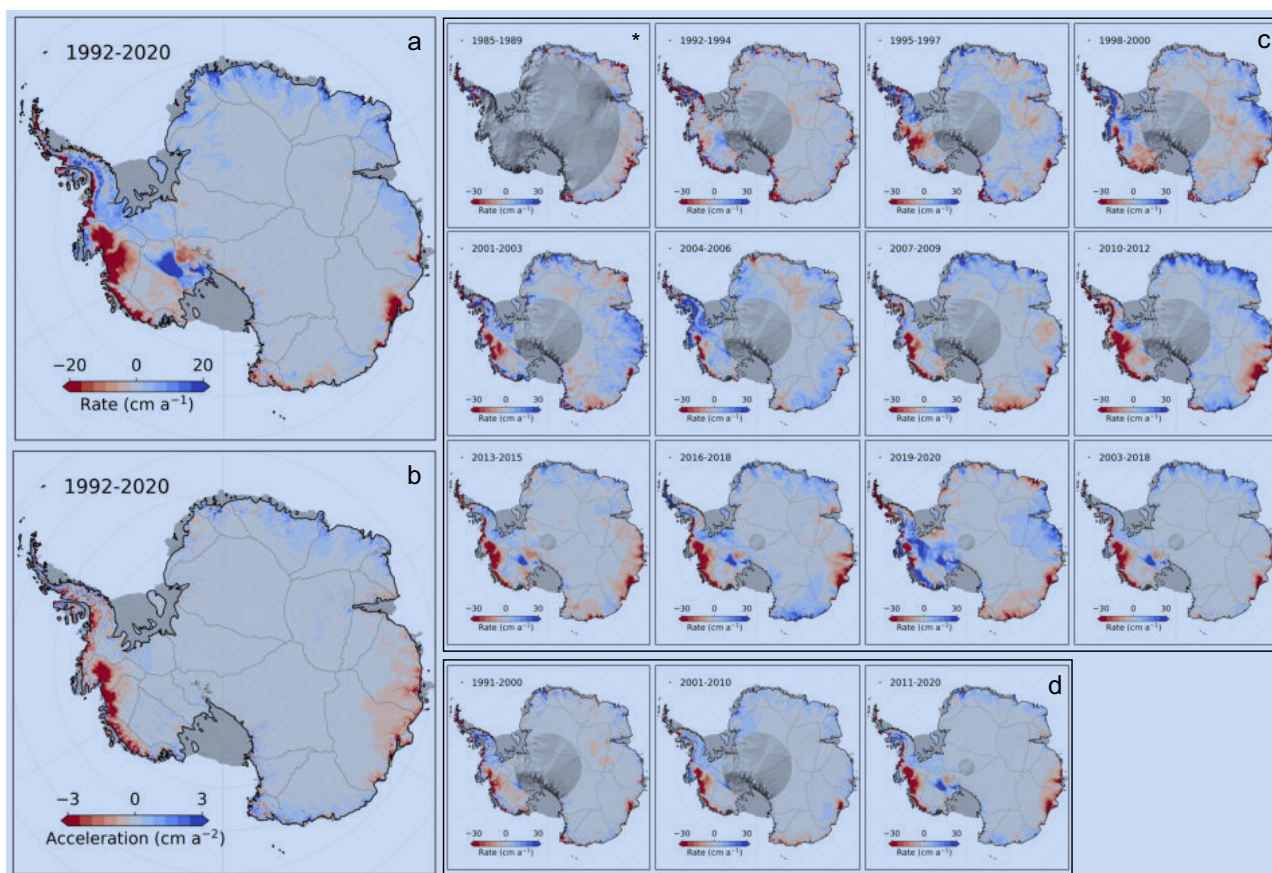
750

751

752 Table 3. Volume change rates spanning 1985 to 2020 for Basins 1-27 (Figure 1) and aggregate regions. Volume  
 753 change errors are computed from the ICESat-ICESat-2 validation procedure, combined with the error in the  
 754 estimated rate.

Regions	1985-1990	1992-1994	1995-1997	1998-2000	2001-2003	2004-2006	2007-2009	2010-2012	2013-2015	2016-2018	2019-2020	1991-2000	2001-2010	2011-2020	2003-2018	1992-2020
1	N/A	-20±16	34±12	34±13	36±13	51±10	16±11	25±9	24±8	30±8	20±10	14±4	23±3	20±3	19±3	20±3
2	N/A	-14±17	12±11	-2±11	31±11	7±7	19±7	-2±6	4±5	3±5	11±5	-6±4	12±3	5±3	4±3	4±3
3	N/A	-7±8	37±6	-34±6	31±7	23±5	21±5	7±5	9±5	3±5	3±6	5±2	32±2	9±2	19±2	15±2
4	3±2	-8±13	11±10	-2±10	17±10	21±8	15±9	11±7	-3±7	7±7	-7±9	3±3	15±2	0±2	11±2	9±2
5	0±5	-3±11	19±8	12±9	15±9	-8±7	30±8	25±6	11±5	10±5	5±7	9±2	5±2	11±2	14±1	10±1
6	13±8	-4±13	4±10	5±11	29±10	-4±9	44±9	75±8	13±7	26±7	5±10	4±3	13±2	16±2	31±2	18±2
7	-18±9	0±13	11±10	16±10	-4±10	17±8	29±9	68±7	11±7	32±6	-13±9	5±3	15±2	13±2	29±2	16±2
8	-1±6	2±12	9±9	7±9	-4±9	7±7	11±7	25±6	1±5	3±5	12±7	3±2	6±2	4±1	10±1	7±1
9	5±5	-4±10	0±7	13±8	-2±8	12±6	4±7	0±5	2±5	-5±5	10±7	2±2	5±2	-3±1	2±1	2±1
10	0±1	-10±7	5±5	-13±5	11±5	-4±4	1±4	16±5	5±5	-3±4	27±6	-9±2	1±2	0±2	3±1	1±1
11	4±3	-8±7	-2±5	8±6	15±6	-3±5	2±5	11±4	-5±4	-5±4	16±5	-1±2	-1±1	-1±1	1±1	2±1
12	-10±7	2±11	19±8	39±8	77±8	7±7	-3±7	12±6	-42±6	-29±6	53±8	4±2	6±2	-26±2	-8±2	7±2
13	-53±9	-6±10	-11±8	-49±8	32±8	28±7	-3±7	-105±6	-60±5	-40±5	-41±8	-13±2	-2±2	-43±2	-31±2	-17±2
14	1±7	-5±10	12±8	23±8	-15±8	30±6	-56±7	45±6	-19±5	56±5	-48±7	3±2	-13±2	11±2	5±1	-1±1
15	-8±18	-42±32	-11±24	-1±25	-2±23	-7±20	-4±22	-3±18	-4±15	12±15	-9±18	-10±6	-8±4	2±3	-2±3	-4±3
16	N/A	-12±10	9±8	-3±8	-4±8	-3±7	-1±7	5±6	-4±6	3±6	0±7	4±2	1±2	2±2	3±1	1±1
17	N/A	-42±19	21±12	-17±11	32±11	-16±8	-1±9	47±8	-9±7	18±7	19±8	4±3	-3±2	8±2	4±2	3±2
18	N/A	26±6	15±5	13±4	32±4	24±3	22±4	25±4	17±3	20±3	40±4	20±3	26±2	24±2	24±2	23±2
19	N/A	4±7	-11±6	-34±6	3±6	11±5	-6±5	-11±5	-5±5	-4±4	9±5	-12±2	1±2	0±1	-4±1	-5±1
20	N/A	-34±26	-29±20	-37±21	-6±21	-14±18	-46±19	-67±13	-39±11	-50±11	26±16	-16±6	-25±5	-32±4	-43±4	-30±4
21	N/A	-31±12	-81±9	-17±9	-73±9	-42±8	-82±8	-113±7	-85±6	-94±6	-8±9	-51±3	-68±2	-78±2	-89±2	-73±2
22	N/A	-8±8	-31±6	-13±6	-28±7	-13±6	-57±6	-90±5	-68±5	-66±5	-2±7	-20±3	-32±3	-58±3	-62±3	-43±3
23	N/A	-3±20	-12±15	18±15	-12±15	19±13	6±14	-25±9	-15±8	-14±8	24±12	-4±4	1±3	-12±2	-12±2	-7±2
24	-5±7	-13±27	8±21	31±22	7±21	41±18	-17±19	-40±13	-7±10	-5±10	3±17	7±5	2±4	-1±3	-12±2	-2±2
25	-45±23	5±23	10±17	-13±18	-26±18	-20±17	-31±18	-45±14	-18±13	8±12	-30±16	-5±8	-21±7	-6±7	-24±7	-20±7
26	43±18	-50±23	-13±17	-14±18	-18±17	-15±16	4±17	-6±12	-10±11	5±11	-22±14	-5±6	-8±5	-5±5	-4±4	-6±4
27	25±9	-6±22	-13±16	13±17	-7±16	11±15	-1±16	-1±11	5±9	-3±9	-5±12	1±4	1±3	1±2	2±2	1±2
EAIS	-64±19	-162±41	143±29	1±30	259±30	108±23	109±25	238±21	-88±19	91±19	43±25	8±8	84±7	7±6	96±6	73±5
AP	18±36	-64±42	-8±31	17±33	-44±32	16±29	-44±31	-93±22	-29±19	5±19	-54±26	-2±11	-26±10	-11±9	-38±8	-27±8
WAIS	N/A	-66±28	-116±21	-36±22	-48±22	36±18	-147±19	-255±16	-170±14	-178±14	109±19	-68±8	-74±7	-135±6	-166±6	-113±6
AIS	-46±26	-292±53	19±39	-18±40	167±40	160±32	-82±34	-110±28	-288±26	-82±25	98±34	-62±14	-16±13	-140±12	-107±11	-68±11

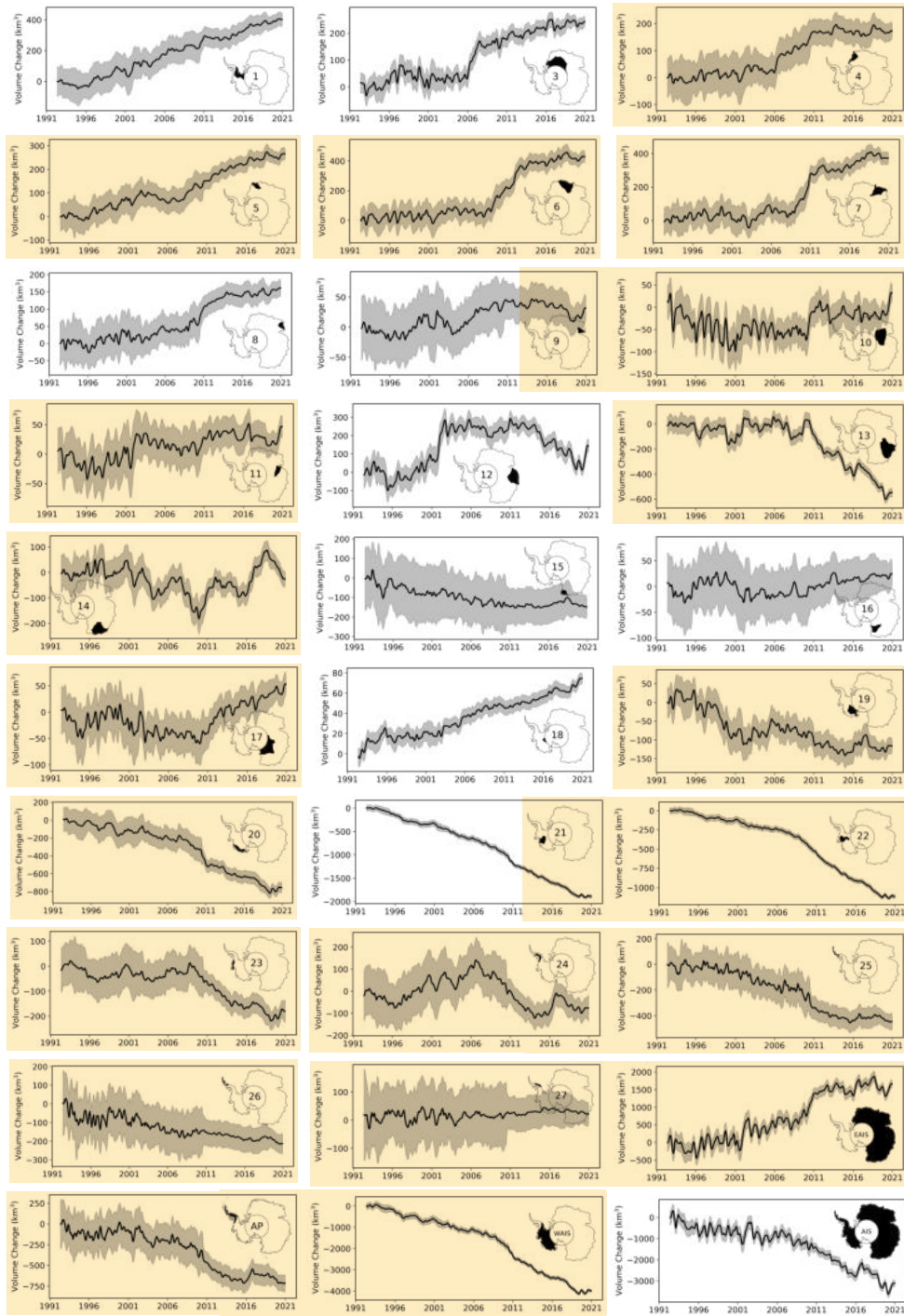
755



756  
 757 Figure 10. Rates of Antarctic Ice Sheet elevation change. Elevation change rate (a) and acceleration (b) for the  
 758 1992-2020 period and average rates for (c) 3-year, (d) ICESat – ICESat-2 and (d) 10-year intervals. (\*) indicates  
 759 a five-year interval for Geosat.

760  
 761 Regionally, concentrated rates of thinning from accelerated glacier flow (Gardner et al., 2018; Rignot et al., 2019)  
 762 are found to spread inland over time due to a regional dynamic imbalance (Shepherd et al., 2019). The marginal  
 763 areas surrounding the Getz ice shelf (Basin 20) also exhibit negative rates of elevation change but are more  
 764 localized to the narrow glacier outlets due to inland topographic barriers and time since initiation of thinning  
 765 (Figure 10-11). This area saw a large break in the overall long-term trend around 2010 when rapid onset thinning  
 766 was observed and attributed to short-term variations in both the surface mass balance and ice dynamics (Chuter  
 767 et al., 2017; Schröder et al., 2019; Gardner et al., 2018). Basin 18, which contains the Kamb Ice Stream,  
 768 experienced a relatively steady gain in volume over the last three decades resulting from the stagnation of the  
 769 Kamb Ice Stream some 200 years prior (Catania et al., 2006) (Figure 10-11). Totten Glacier (Basin 13), part of  
 770 the EAIS, has been losing mass since the late 1970's (Schröder et al., 2019) with the average trend mostly governed  
 771 by ice dynamics and short-term variability and acceleration driven by changes in precipitation (Li et al., 2016). A  
 772 major change in trend was observed in 2010 when a large-scale thinning of the entire is observed, likely in  
 773 response to a change in precipitation and possibly changes ice dynamic driven by changes in ocean conditions  
 774 (Khazendar et al., 2013; Li et al., 2016). The activation or reversal in trend of both the Totten and Denman glaciers  
 775 in early 2009-2010 has disrupted the long-term equilibrium or gain that has been observed for most parts of Wilkes  
 776 Land (Basins 12 and 13, Figure 1). A departure from the long-term trend can now be observed for large parts of  
 777 Wilkes Land in the form of large-scale negative acceleration spreading inland (Figure 10). In Dronning Maud

778 Land and Enderby Land (Basins 5-8), the previously mentioned snow-fall events in 2009 and 2011 (Boening et  
779 al., 2012) are clearly observed in the regional elevation change trends. This pattern is most prominent along the  
780 Weddell Sea coast where the accumulation signal, in the form of precipitation, shows an earlier event in 2006  
781 (Basins 3 and 4) (Figure 10 and 11). The glaciers flowing into the Bellingshausen Sea have shown a complex  
782 pattern of change over the last 29 years. Here, Palmer Land (Basin 24) shows a steady increase in surface elevation  
783 over the initial 15 years of the record, following a long-term positive anomaly in precipitation from 1992.  
784 However, a reversal in this pattern was observed around 2007 where patterns of thinning (McMillan et al., 2014;  
785 Schröder et al., 2019; Shepherd et al., 2019; Wouters et al., 2015) (Figure 10) can be observed localized to the  
786 major low-elevation outlet glaciers in the regions. The change can be largely attributed to a change in precipitation  
787 amount, with lesser contributions from changes in ice dynamics resulting from enhanced melting by the ocean  
788 (Gardner et al., 2018; Hogg et al., 2017). However, in the southern part of the Bellingshausen Sea, near Ferrigno  
789 glacier in Basin 23, we find a relatively stable trend during most of the record until 2009 when a large acceleration  
790 in ice loss can be observed. This acceleration can only be partially attributed to changes in ice dynamics (Gardner  
791 et al., 2018; Wouters et al., 2015) and it is likely that changes in precipitation is the major driver of change. Large  
792 changes in both spatial and temporal variability can be observed in the AP region in the last three decades, where  
793 large scale reversals of signals can be observed over different time periods. Here, we find a large-scale positive  
794 elevation change anomaly in Basin 23-26, superimposed on a long-term negative trend, over the time periods  
795 1998-2000, 2004-2006 and 2016-2018. These changes are linked to changes in the short-term variability of SMB  
796 in the region due to increased precipitation. Examining the rates derived over the ICESat-2 time period (2018-  
797 2020) a large positive elevation change signal can be observed over the WAIS region, in contrast to the overall  
798 negative long-term trend. This anomaly is directly linked to large scale snow-accumulation, resulting from an  
799 extreme precipitation event in the austral winter of 2019 which has been attributed to the landfall of atmospheric  
800 rivers (Adusumilli et al., 2021).



801  
 802 Figure 11. Basin (Zwally et al., 2012) and ice sheet monthly elevation change time series for the period of 1992  
 803 to 2020.

804  
 805  
 806

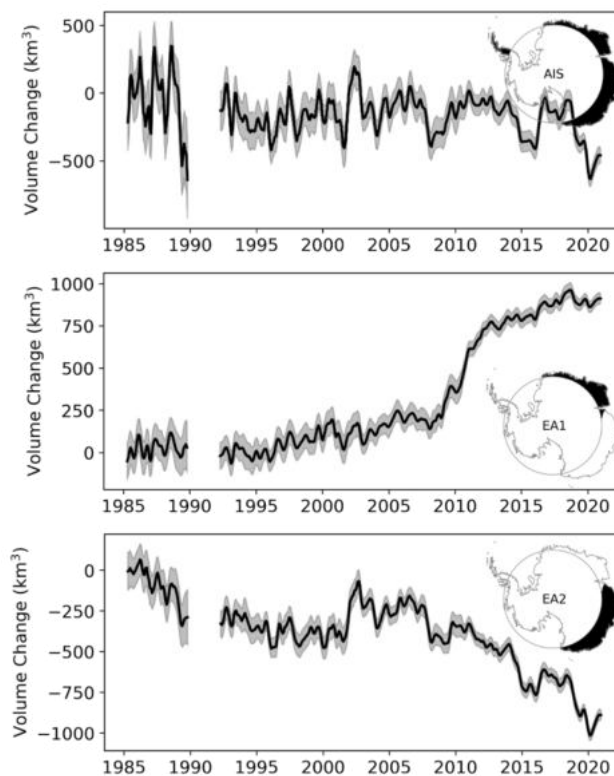
## 807 6 Discussion

808 We provide a new elevation change product for the Antarctic Ice Sheet that synthesizes over three decades of data  
809 from seven different satellite altimeters. To do this we applied slope corrections to all pulse-limited radar altimetry  
810 datasets, substantially reducing the overall error in both measured elevation and elevation change rates as can be  
811 seen in the crossover quality analysis. Our methodology explicitly separates the time-variable and the static  
812 topography in the inversion for elevation change and is one of the major improvements over previous studies  
813 (Flament et al., 2012; McMillan et al., 2014; Moholdt et al., 2010). Removing the time-invariant topography from  
814 the time-variable elevation allowed us to more easily accommodate varying spatial scales of correlation inherent  
815 to the different processes affecting the altimetry retrievals of elevation. This can be conceptualized by noting that  
816 correlation lengths are less than <10 km for the time-invariant topography, while elevation change signal are  
817 correlated at length scales greater than 50 km in some places. We performed extensive testing over Lake Vostok  
818 in East Antarctica and concluded that the optimum search radius for estimating time-invariant topography was  
819 500 m for repeat track missions and 1000 m for drifting-track missions. An extensive investigation was also  
820 undertaken to determine the optimum radius for maximizing correlation between the waveform parameters and  
821 the time-variable elevation change. From this analysis it was determined that a 1000 m search radius provided the  
822 best results in both minimizing the trend and RMS of the residuals. Both spatial and temporal patterns of changes  
823 in the scattering horizon (penetration depth) (Figure 2 and 3) of the radar signal further highlights the importance  
824 of this correction, which can reach magnitudes of several  $\text{cm a}^{-1}$  (Figure 3). This correction also has a significant  
825 impact on the magnitude of the seasonal signal at continent wide scales and can produce reduction of upwards of  
826 50% in the seasonal amplitude of the elevation change signal (Figure 3 and 5).

827

828 Cross-calibration of the different missions is likely the most challenging barrier to generating a continuous and  
829 accurate record of elevation change. In this study we have taken a somewhat different approach to Schröder et al.  
830 (2019) and Shepherd et al. (2019). Here, we work entirely in residual space, after the removal of time-invariant  
831 topography. We first apply a least-squares approach to provide an initial inter-mission adjustment. This  
832 adjustment is mainly to align overlapping data and modes such as ICESat and Envisat. The approach also has  
833 advantages of removing long-term trends and seasonality, allowing us to estimate any remaining offset by  
834 examining the residuals to the least-squares model. We find here that the Envisat and CryoSat-2 transition is  
835 troublesome, as only a few months of data overlap exist due to the later change in orbit of the Envisat mission and  
836 the large ice sheet-wide changes that occur around this transition. To overcome the sampling problem and the  
837 variable elevation change behavior observed for different locations, we investigated several methods to estimate  
838 Envisat/CryoSat-2 offsets. Given the availability of high-accuracy ICESat and ICESat-2 elevation change rates  
839 we were able to determine which offset provided the most appropriate trend compared to the laser altimetry  
840 reference. One should note that we do not use the laser altimetry data to scale or generate the offset, its merely an  
841 independent guide to select the most suitable offset produced from the different alignment approaches. This  
842 method provides volume changes that are well in line with both the CPOM and TUD products, which provides us  
843 with confidence in our approach. Further, it is unfortunate that Envisat changes orbit in late 2010 as it would have  
844 allowed almost 2 years of overlap with CryoSat-2. Hopefully this data can be included in the future versions once  
845 the issue of how to satisfactorily handle the change in orbit can be addressed. This work is currently being  
846 undertaken. As of now, including post orbit change data in the synthesis has the effect of introducing noise in the

847 Envisat time series and spurious offsets, severely limiting the use of the data. For the Geosat data we include a  
 848 caveat for the quality of the cross-calibration. A cross-calibration has been applied but the quality of this  
 849 adjustment can vary due to the long gap separation between Geosat (ending in 1990) and the next altimetry mission  
 850 (ERS-1: starting in 1992). We recommend that care be taken here and suggest that for regional studies that a  
 851 manual post-calibration be applied. The suggestion would be to follow the approach outlined in Sect. 3.2.3 using  
 852 Eq. (2) varying the degree of the polynomial until satisfactory results are obtained, as seen in Fig. 12.  
 853



854  
 855 Figure 12. Monthly elevation change time series for the area measured by Geosat (72° S latitude limit) for the  
 856 period 1985-2020. The large difference in RMS seen in the Geosat time series for full ice sheet is mostly driven  
 857 by observations collected over the Antarctic Peninsula. The regional Geosat time series were recalibrated to  
 858 allow for better alignment with the long-term record, as suggested in Section 6. This as the local offset estimated  
 859 at each grid-cell for Geosat might not be of sufficient quality everywhere.

860  
 861 Another important altimetry correction in the processing is the amplitude normalization, using CryoSat-2 as a  
 862 reference. Fig. 5 illustrates that even after applying corrections for the change in scattering horizon (e.g.,  
 863 penetration bias), the different missions show inconsistent seasonal amplitudes with the older pulse-limited  
 864 mission that have seasonal amplitudes that are more than twice that of newer missions (e.g., Envisat, CryoSat-2,  
 865 and ICESat/2). This is most likely linked to the higher level of noise in the older sensors (~30 cm vs ~10 cm). The  
 866 larger noise levels make it difficult to separate the change in a shifting scattering horizon with time-invariant  
 867 topography. Hence, there is need to normalize the different seasonal amplitudes over the different missions, as  
 868 there is no physical justification for why they should differ. Here we found that both the ICESat and CryoSat-2  
 869 mission showed remarkable good agreement in seasonal amplitude with surface elevation change simulated by  
 870 the RACMO firn densification model (Ligtenberg et al., 2012). In the end we selected CryoSat-2 as the reference,



871 as it provides both higher spatial and temporal sampling compared to ICESat. ICESat-2 was not considered as we  
872 believe that the record currently is too short (only 2 years was used in this study) to provide a viable estimate of  
873 seasonal climatology. It should be noted that this correction removes the mean difference in amplitude between  
874 missions but does not modulate the seasonal-phase or the inter-annual variability in the amplitude within a single  
875 mission.

876  
877 Large data gaps exist at latitudes exceeding the maximum orbital coverage; this gap is referred to as the pole hole.

878 In our product we fill the pole hole to provide a spatially complete field to aid in the estimation of ice sheet wide  
879 mass balance and to make the data more usable for modeling efforts. However, we do recognize that our chosen  
880 interpolation method may not be appropriate for regions such as AP and Basins 15-17, which are comprised of  
881 highly variable topography. Therefore, we provide a mask layer (*data\_flag*) that identifies *high quality, low*  
882 *quality* (high topographic relief), and *pole hole* data. After some investigation we found that applying the  
883 hypsometry method to extrapolating monthly estimates of elevation change produced an improved estimate of  
884 basin scale volume changes when compared to the ICESat-ICESat-2 product. This methodology is not applied to  
885 distributed product. We leave it up to the user of the product to apply their own methodology for extrapolation,  
886 but we recommend that the hypsometric method when generating basin scale mass balance estimates.

887  
888 Elevation change rates near the pole hole are relatively small, due to low precipitation amounts (Wingham et al.,  
889 2006) and few dynamically active glaciers. Changes in mass within the pole hole only amount to few tens of  
890 gigatons of change (Shepherd et al., 2019), once corrected for firn-air-content. Hence, the interpolation of data to  
891 fill the pole hole only contributes a small part of the overall volume change. In our estimate the overall volume  
892 change is estimated to be  $26 \text{ km}^3 \text{ a}^{-1}$  South of  $81.5^\circ \text{ S}$  over the full 2003-2018 time period using the least-squares  
893 adjustment method and  $34 \text{ km}^3 \text{ a}^{-1}$  when adding the residual cross-calibration. This aligns well with the value  
894 estimated from the ICESat-ICESat-2 product of  $37 \text{ km}^3 \text{ a}^{-1}$  for the area  $81.5^\circ\text{-}86^\circ \text{ S}$  over the period 2003-2019.  
895 Studying the other two publicly available altimetry synthesis we find that their pole-hole volume estimates are  
896 biased in the negative direction (compared to the ICESat-ICESat-2 product) and can be quite large: -65 (CPOM)  
897 and -12 (TUD)  $\text{km}^3\text{a}^{-1}$ . This indicates that using either a constant offset or mission-only derived trends for cross-  
898 calibration might not be sufficient for these areas, as a small error can have a large impact when integrated over  
899 a large region. This further points to the effectiveness of using the least-squares adjustment for cross-calibrating non-  
900 overlapping records.

901  
902 Previous altimetry studies of Antarctic mass balance have relied heavily on airborne laser altimetry to provide  
903 validation and estimates of the overall volume change uncertainty (McMillan et al., 2014; Wouters et al., 2015).  
904 However, airborne data are both limited in spatial and temporal coverage, making it extremely difficult to estimate  
905 volume change uncertainties on continental scales. We, for the first time, have used long-term (16-years) unbiased  
906 laser altimetry derived rates of elevation change from Smith et al. (2020) to produce ice sheet wide uncertainties  
907 for our product. This is especially important for East Antarctica where very little validation data exists from either  
908 in-situ or airborne campaigns. Though the rates here are on the order of cm per year, they occur over massive  
909 spatial scales and contribute significantly to the overall ice sheet volume change. 16-years of high-accuracy laser  
910 data allows us to validate these cm trends as the measurement error reduces as a function of time. This dataset

911 allows us to quantify and validate changes at the  $\text{mm a}^{-1}$  level, which was previously not possible in East  
912 Antarctica. The overall uncertainty estimates of  $-0.8 \pm 7.8 \text{ mm a}^{-1}$  is heavily dominated by the small difference in  
913 the interior areas of the ice sheet, which rapidly increase closer to the coast with errors reaching  $25 \text{ mm a}^{-1}$ . In  
914 general, the analysis shows that radar altimeters underperform, relative to laser altimeters, in areas of steep  
915 topography where change signals are largest. Further, we observe that in East Antarctica, the radar record in many  
916 places produces small negative rates, compared to slightly positive rates from laser, indicating residual issues with  
917 time-variable radar penetration biases. These issues are of course known to the scientific community (Arthern et  
918 al., 2001; Davis, 1993; Lacroix et al., 2009; Legresy and Remy, 1997; Nilsson et al., 2015a) and is an area of  
919 active research. However, with this new laser altimetry dataset we now have at least the possibility of quantifying  
920 this type of uncertainty across nearly the entirety of the ice sheet.

921  
922 Comparing the estimate from this study with the TUD (Schröder et al. 2019) and CPOM (Shepherd et al., 2019)  
923 products we find good agreement over the 1992-2016 time period, with differences within the error budgets of  
924 the respective products. This agreement is a good indicator that all three products provide consistent results given  
925 the different processing methodologies for areas below  $81.5^\circ \text{ S}$ . Analyzing further, we find that the main  
926 difference between products is in the overall noise levels. Given the different comparisons we find that, on  
927 average, our product has lower noise and agrees most closely with the laser-altimetry validation data. We attribute  
928 this improvement in noise characteristics to the improved processing techniques.

929  
930 Another, important improvement is the normalization of the seasonal signal across missions. Though this  
931 correction is not perfect, it has lowered the magnitude of the average seasonal signal to a level comparable to the  
932 simulated values of elevation change from the RACMO FDM product (Ligtenberg et al., 2012). Accurate  
933 quantification of the “seasonal breathing” of the Antarctic ice sheet is important component to estimated rates of  
934 snowfall. However, we do find discrepancy between the altimetric and modelled rates of change for East  
935 Antarctica, with rates of change differing in places by 200% to 300% for the 1992-2016 period. We further find  
936 that the direction of change can have opposite sign between modeled and observed rates, as can be seen in the  
937 Wilkes Land region. This indicates that the current generation of firm densification models, though highly  
938 successful in representing the main components governing ice sheet mass balance, still cannot fully capture all  
939 the complex interactions driving changes in surface elevation. This of course has large implications for estimating  
940 the East Antarctica mass balance as the correction for firm-air-content can be as large as 100% of the measured  
941 altimetry signal in some basins (Smith et al., 2020). However, several new firm models are expected to become  
942 available within the near future, which will greatly help the community to quantify both the error in these models  
943 and to help improve our understanding of the processes driving the ice sheet mass balance.

944

945

946

947

948

949

## 950 7 Data and code availability

951 Data can be found at [Nilsson et al., 2021; <https://doi.org/10.5067/L3LSVDZS15ZV>]. The code and algorithm  
952 used to generate the product are part of the “Cryosphere Altimetry Processing Toolkit” (captoolkit) and can be  
953 found here: <https://github.com/nasa-jpl/captoolkit>

## 954 8 Summary and conclusion

955 In this study we have provided a 36-year record (1985-2020) of elevation change for the Antarctic ice sheet  
956 derived from seven altimetry missions combining both laser and radar measurements. Elevation changes were  
957 derived from measurements of surface elevation by first removing the time-invariant topography for each mission  
958 and applying corrections for varying surface scattering characteristics that affect radar altimetry. The different  
959 sensors and modes were cross-calibrated and merged into a continuous record of elevation change, using a  
960 combination of interpolation and extrapolation techniques to construct a consistent spatiotemporal dataset for the  
961 scientific community.

962

963 Our dataset indicates that between 1992 and the later parts of 2000’s, the Antarctic ice sheet was in near balance,  
964 with modest EAIS gains equaling WAIS losses. In the later parts of the 2000’s accelerated WAIS losses outpaced  
965 EAIS gains, leading to significant net decrease in ice sheet volume. This accelerated loss has been attributed to  
966 increased ocean melting and changes in precipitation (Shepherd et al., 2018). East Antarctica has also seen  
967 changes over the last 30 years, where large swaths of Wilkes Land are now showing accelerating negative  
968 elevation change starting around the year 2010 and likely stemming from changes in precipitation/firn, and  
969 possibly ice dynamics from the Denman and Totten glacier systems. The Dronning Maud Land region has started  
970 to show extensive elevation gain due to significant increases in snowfall beginning around 2009. However, one  
971 of the main questions still remains: is EAIS losing or gaining mass? With these long-term improved datasets, in  
972 combination with accurate firn-modelling, we may soon be able to answer this question. The western parts of  
973 Antarctica have seen both consistent and accelerated mass loss over the entire altimetry record dominated by the  
974 glacier systems of Pine Island and Thwaites. These areas now show drawdowns for hundreds of kilometers inland,  
975 and currently show no signs of slowing down. The Antarctic Peninsula also shows signals of major mass loss, but  
976 the long-term accuracy of those estimates is hard to quantify due to inherent limitations of radar measurements  
977 over these types of rugged terrain. We can, however, say with confidence that large changes due to a complex  
978 mix of atmosphere and ocean forcing have accelerated mass loss in the Bellingshausen Sea over the length of the  
979 record (Gardner et al., 2018; Hogg et al., 2017; Wouters et al., 2015). This region was relatively stable for two  
980 decades but started to show a large change in behavior from its original trend in the 2008-2010 period.

981

982 It is our hope that the newly produced ITS\_LIVE synthesized record of Antarctic Ice Sheet elevation change will  
983 improve understanding of the underlying processes driving the patterns of elevation change, with the hope that  
984 such understanding will lead to improved projections of ice sheet and sea level change.

985

986 **Competing interests**

987 The authors declare that they have no conflict of interest.

988

989 **Author contributions**

990 J.N. and A.S.G. conceptualized the study. J.N. conducted the analysis, wrote the majority of the main text and  
991 made all figures. J.N., A.S.G. and F.S.P all contributed to conceptualization and algorithms development. All  
992 authors contributed to the writing and editing of the manuscript.

993

994 **Financial support**

995 The authors were supported by the NASA MEaSUREs, and the NASA Cryosphere Science Program  
996 (NNH16ZDA001N-ICESAT2), and the Jet Propulsion Laboratory, California Institute of Technology, through an  
997 agreement with the National Aeronautics and Space Administration.

998 **Acknowledgements**

999 The authors were supported by the ITS\_LIVE project awarded through NASA MEaSUREs program, and the  
1000 NASA Cryosphere program through participation in the ICESat-2 science team. We thank the NASA and the  
1001 European Space Agency (ESA) for distributing their radar altimetry data. The author would like to thank Sebastian  
1002 Bjerregaard Simonsen for the discussions and data support during the early part of the study, it was immensely  
1003 helpful. Further, we would also like to thank Ludwig Schröder for his help with obtaining the Geosat, data and  
1004 Veit Helm and the anonymous reviewer for their helpful comments which greatly improved the manuscript. The  
1005 research described in this paper was carried out at the Jet Propulsion Laboratory, California Institute of  
1006 Technology, under a contract with NASA.

1007

1008

1009

1010

1011

1012

1013

1014

1015

1016

1017

1018

1019

1020

1021

1022

1023 **References**

- 1024 Adusumilli, S., Fish, M., Fricker, H. A. and Medley, B.: Atmospheric River Precipitation Contributed to Rapid  
1025 Increases in Surface Height of the West Antarctic Ice Sheet in 2019, *Geophys. Res. Lett.*, 48(5),  
1026 doi:10.1029/2020GL091076, 2021.
- 1027 Armitage, T. W. K., Wingham, D. J. and Ridout, A. L.: Meteorological Origin of the Static Crossover Pattern  
1028 Present in Low-Resolution-Mode CryoSat-2 Data Over Central Antarctica, *IEEE Geosci. Remote Sens. Lett.*,  
1029 11(7), 1295–1299, doi:10.1109/LGRS.2013.2292821, 2014.
- 1030 Arthern, R., Wingham, D. and Ridout, A.: Controls on ERS altimeter measurements over ice sheets: **Footprint-**  
1031 scale topography, backscatter fluctuations, and the dependence of microwave penetration depth on satellite  
1032 orientation, *J. Geophys. Res. Atmos.*, 106(D24), 33471–33484, doi:10.1029/2001JD000498, 2001.
- 1033 Bamber, J. L.: Ice sheet altimeter processing scheme, *Int. J. Remote Sens.*, 15(4), 925–938,  
1034 doi:10.1080/01431169408954125, 1994.
- 1035 Bevis, M. and Brown, A.: Trajectory models and reference frames for crustal motion geodesy, *J. Geod.*, 88(3),  
1036 283–311, doi:10.1007/s00190-013-0685-5, 2014.
- 1037 Boening, C., Lebsock, M., Landerer, F. and Stephens, G.: Snowfall-driven mass change on the East Antarctic  
1038 ice sheet, *Geophys. Res. Lett.*, 39(21), n/a-n/a, doi:10.1029/2012GL053316, 2012.
- 1039 Borsa, A. A., Moholdt, G., Fricker, H. A. and Brunt, K. M.: A range correction for ICESat and its potential  
1040 impact on ice-sheet mass balance studies, *Cryosphere*, 8(2), 345–357, doi:10.5194/tc-8-345-2014, 2014.
- 1041 Borsa, A. A., Fricker, H. A. and Brunt, K. M.: A Terrestrial Validation of ICESat Elevation Measurements and  
1042 Implications for Global Reanalyses, *IEEE Trans. Geosci. Remote Sens.*, 57(9), 6946–6959,  
1043 doi:10.1109/TGRS.2019.2909739, 2019.
- 1044 Brenner, A. C., Blndschadler, R. A., Thomas, R. H. and Zwally, H. J.: Slope-induced errors in radar altimetry  
1045 over continental ice sheets, *J. Geophys. Res.*, 88(C3), 1617, doi:10.1029/JC088iC03p01617, 1983.
- 1046 Brenner, A. C., DiMarzio, J. P. and Zwally, H. J.: Precision and Accuracy of Satellite Radar and Laser Altimeter  
1047 Data Over the Continental Ice Sheets, *IEEE Trans. Geosci. Remote Sens.*, 45(2), 321–331,  
1048 doi:10.1109/TGRS.2006.887172, 2007.
- 1049 Brockley, D. J., Baker, S., Femenias, P., Martinez, B., Massmann, F. H., Otten, M., Paul, F., Picard, B., Prandi,  
1050 P., Roca, M., Rudenko, S., Scharroo, R. and Visser, P.: REAPER: Reprocessing 12 Years of ERS-1 and ERS-2  
1051 Altimeters and Microwave Radiometer Data, *IEEE Trans. Geosci. Remote Sens.*, 55(10), 5506–5514,  
1052 doi:10.1109/TGRS.2017.2709343, 2017.
- 1053 Brunt, K. M., Hawley, R. L., Lutz, E. R., Studinger, M., Sonntag, J. G., Hofton, M. A., Andrews, L. C. and  
1054 Neumann, T. A.: Assessment of NASA airborne laser altimetry data using ground-based GPS data near Summit  
1055 Station, Greenland, *Cryosph.*, 11(2), 681–692, doi:10.5194/tc-11-681-2017, 2017.
- 1056 Catania, G. A., Scambos, T. A., Conway, H. and Raymond, C. F.: Sequential stagnation of Kamb Ice Stream,  
1057 West Antarctica, *Geophys. Res. Lett.*, 33(14), L14502, doi:10.1029/2006GL026430, 2006.
- 1058 Chuter, S. J., Martín-Español, A., Wouters, B. and Bamber, J. L.: Mass balance reassessment of glaciers  
1059 draining into the Abbot and Getz Ice Shelves of West Antarctica, *Geophys. Res. Lett.*, 44(14), 7328–7337,  
1060 doi:10.1002/2017GL073087, 2017.
- 1061 Davis, C. H.: Surface and volume scattering retracking algorithm for ice sheet satellite altimetry, *IEEE Trans.*  
1062 *Geosci. Remote Sens.*, 31(4), 811–818, doi:10.1109/36.239903, 1993.

- 1063 Davis, C. H.: Temporal Change in the Extinction Coefficient of Snow on the Greenland Ice Sheet from an  
1064 Analysis of Seasat and Geosat Altimeter Data, *IEEE Trans. Geosci. Remote Sens.*, 34(5), 1066–1073,  
1065 doi:10.1109/36.536522, 2000.
- 1066 Davis, C. H.: Snowfall-Driven Growth in East Antarctic Ice Sheet Mitigates Recent Sea-Level Rise, *Science*  
1067 (80-. ), 308(5730), 1898–1901, doi:10.1126/science.1110662, 2005.
- 1068 Davis, C. H. and Ferguson, A. C.: Elevation change of the Antarctic ice sheet, 1995-2000, from ERS-2 satellite  
1069 radar altimetry, *IEEE Trans. Geosci. Remote Sens.*, 42(11), 2437–2445, doi:10.1109/TGRS.2004.836789, 2004.
- 1070 Davis, J. L., Wernicke, B. P. and Tamisiea, M. E.: On seasonal signals in geodetic time series, *J. Geophys. Res.*  
1071 *Solid Earth*, 117(1), 1–10, doi:10.1029/2011JB008690, 2012.
- 1072 Flament, T. and Rémy, F.: Dynamic thinning of Antarctic glaciers from along-track repeat radar altimetry, *J.*  
1073 *Glaciol.*, 58(211), 830–840, doi:10.3189/2012JoG11J118, 2012.
- 1074 Fretwell, P., Pritchard, H. D., Vaughan, D. G., Bamber, J. L., Barrand, N. E., Bell, R., Bianchi, C., Bingham, R.  
1075 G., Blankenship, D. D., Casassa, G., Catania, G., Callens, D., Conway, H., Cook, A. J., Corr, H. F. J., Damaske,  
1076 D., Damm, V., Ferraccioli, F., Forsberg, R., Fujita, S., Gim, Y., Gogineni, P., Griggs, J. A., Hindmarsh, R. C.  
1077 A., Holmlund, P., Holt, J. W., Jacobel, R. W., Jenkins, A., Jokat, W., Jordan, T., King, E. C., Kohler, J., Krabill,  
1078 W., Riger-Kusk, M., Langley, K. A., Leitchenkov, G., Leuschen, C., Luyendyk, B. P., Matsuoka, K., Mouginot,  
1079 J., Nitsche, F. O., Nogi, Y., Nost, O. A., Popov, S. V., Rignot, E., Rippin, D. M., Rivera, A., Roberts, J., Ross,  
1080 N., Siegert, M. J., Smith, A. M., Steinhage, D., Studinger, M., Sun, B., Tinto, B. K., Welch, B. C., Wilson, D.,  
1081 Young, D. A., Xiangbin, C. and Zirizzotti, A.: Bedmap2: Improved ice bed, surface and thickness datasets for  
1082 Antarctica, *Cryosphere*, 7(1), 375–393, doi:10.5194/tc-7-375-2013, 2013.
- 1083 Gardner, A. S., Moholdt, G., Scambos, T., Fahnestock, M., Ligtenberg, S., van den Broeke, M. and Nilsson, J.:  
1084 Increased West Antarctic and unchanged East Antarctic ice discharge over the last 7 years, *Cryosph.*, 12(2),  
1085 521–547, doi:10.5194/tc-12-521-2018, 2018.
- 1086 Gardner, A. S., M. A. Fahnestock, and T. A. Scambos, 2019 [update to time of data download]: ITS\_LIVE  
1087 Regional Glacier and Ice Sheet Surface Velocities. Data archived at National Snow and Ice Data Center;  
1088 doi:10.5067/6II6VW8LLWJ7.
- 1089 Groh, A. and Horwath, M.: Antarctic Ice Mass Change Products from GRACE/GRACE-FO Using Tailored  
1090 Sensitivity Kernels, *Remote Sens.*, 13(9), 1736, doi:10.3390/rs13091736, 2021.
- 1091 Helm, V., Humbert, A. and Miller, H.: Elevation and elevation change of Greenland and Antarctica derived  
1092 from CryoSat-2, *Cryosph.*, 8(4), 1539–1559, doi:10.5194/tc-8-1539-2014, 2014.
- 1093 Herzfeld, U. C.: Least-squares collocation, geophysical inverse theory and geostatistics: a bird's eye view,  
1094 *Geophys. J. Int.*, 111(2), 237–249, doi:10.1111/j.1365-246X.1992.tb00573.x, 1992.
- 1095 Hogg, A. E., Shepherd, A., Cornford, S. L., Briggs, K. H., Gourmelen, N., Graham, J. A., Joughin, I., Mouginot,  
1096 J., Nagler, T., Payne, A. J., Rignot, E. and Wuite, J.: Increased ice flow in Western Palmer Land linked to ocean  
1097 melting, *Geophys. Res. Lett.*, 44(9), 4159–4167, doi:10.1002/2016GL072110, 2017.
- 1098 Holland, P. W. and Welsch, R. E.: Robust regression using iteratively reweighted least-squares, *Commun. Stat.*  
1099 *- Theory Methods*, 6(9), 813–827, doi:10.1080/03610927708827533, 1977.
- 1100 Hurkmans, R. T. W. L., Bamber, J. L., Sørensen, L. S., Joughin, I. R., Davis, C. H. and Krabill, W. B.:  
1101 Spatiotemporal interpolation of elevation changes derived from satellite altimetry for Jakobshavn Isbrae,  
1102 Greenland, *J. Geophys. Res. Earth Surf.*, 117(F3), n/a-n/a, doi:10.1029/2011JF002072, 2012.

- 1103 Joughin, I., Smith, B. E. and Medley, B.: Marine Ice Sheet Collapse Potentially Under Way for the Thwaites  
 1104 Glacier Basin, West Antarctica, *Science* (80-. ), 344(6185), 735–738, doi:10.1126/science.1249055, 2014.
- 1105 Kalman, R. E.: A New Approach to Linear Filtering and Prediction Problems, *J. Basic Eng.*, 82(1), 35,  
 1106 doi:10.1115/1.3662552, 1960.
- 1107 Khazendar, A., Schodlok, M. P., Fenty, I., Ligtenberg, S. R. M., Rignot, E. and van den Broeke, M. R.:  
 1108 Observed thinning of Totten Glacier is linked to coastal polynya variability, *Nat. Commun.*, 4(1), 2857,  
 1109 doi:10.1038/ncomms3857, 2013.
- 1110 Khvorostovsky, K. S.: Merging and Analysis of Elevation Time Series Over Greenland Ice Sheet From Satellite  
 1111 Radar Altimetry, *IEEE Trans. Geosci. Remote Sens.*, 50(1), 23–36, doi:10.1109/TGRS.2011.2160071, 2012.
- 1112 Konrad, H., Gilbert, L., Cornford, S. L., Payne, A., Hogg, A., Muir, A. and Shepherd, A.: Uneven onset and  
 1113 pace of ice-dynamical imbalance in the Amundsen Sea Embayment, West Antarctica, *Geophys. Res. Lett.*,  
 1114 44(2), 910–918, doi:10.1002/2016GL070733, 2017.
- 1115 Lacroix, P., Legresy, B., Remy, F., Blarel, F., Picard, G. and Brucker, L.: Rapid change of snow surface  
 1116 properties at Vostok, East Antarctica, revealed by altimetry and radiometry, *Remote Sens. Environ.*, 113(12),  
 1117 2633–2641, doi:10.1016/j.rse.2009.07.019, 2009.
- 1118 Legresy, B. and Remy, F. R.: Surface characteristics of the Antarctic ice sheet and altimetric observation, *J.*  
 1119 *Glaciol.*, 43(144), 1–11, 1997.
- 1120 Li, X., Rignot, E., Mouginot, J. and Scheuchl, B.: Ice flow dynamics and mass loss of Totten Glacier, East  
 1121 Antarctica, from 1989 to 2015, *Geophys. Res. Lett.*, 43(12), 6366–6373, doi:10.1002/2016GL069173, 2016.
- 1122 Li, Y. and Davis, C. H.: Improved Methods for Analysis of Decadal Elevation-Change Time Series Over  
 1123 Antarctica, *IEEE Trans. Geosci. Remote Sens.*, 44(10), 2687–2697, doi:10.1109/TGRS.2006.871894, 2006.
- 1124 Ligtenberg, S. R. M., Horwath, M., van den Broeke, M. R. and Legrésy, B.: Quantifying the seasonal  
 1125 “breathing” of the Antarctic ice sheet, *Geophys. Res. Lett.*, 39(23), n/a-n/a, doi:10.1029/2012GL053628, 2012.
- 1126 MacGregor, Joseph A., Linette N. Boisvert, Brooke Medley, Alek A. Petty, Jeremy P. Harbeck, Robin E. Bell,  
 1127 J. Bryan Blair et al. "The scientific legacy of NASA's Operation IceBridge." *Reviews of Geophysics* 59, no. 2  
 1128 (2021).
- 1129 Markus, T., Neumann, T., Martino, A., Abdalati, W., Brunt, K., Csatho, B., Farrell, S., Fricker, H., Gardner, A.,  
 1130 Harding, D., Jasinski, M., Kwok, R., Magruder, L., Lubin, D., Luthcke, S., Morison, J., Nelson, R.,  
 1131 Neuenschwander, A., Palm, S., Popescu, S., Shum, C. K., Schutz, B. E., Smith, B., Yang, Y. and Zwally, J.: The  
 1132 Ice, Cloud, and land Elevation Satellite-2 (ICESat-2): Science requirements, concept, and implementation,  
 1133 *Remote Sens. Environ.*, 190, 260–273, doi:10.1016/j.rse.2016.12.029, 2017.
- 1134 McMillan, M., Shepherd, A., Sundal, A., Briggs, K., Muir, A., Ridout, A., Hogg, A. and Wingham, D.:  
 1135 Increased ice losses from Antarctica detected by CryoSat-2, *Geophys. Res. Lett.*, 41(11), 3899–3905,  
 1136 doi:10.1002/2014GL060111, 2014.
- 1137 Moholdt, G., Nuth, C., Hagen, J. O. and Kohler, J.: Recent elevation changes of Svalbard glaciers derived from  
 1138 ICESat laser altimetry, *Remote Sens. Environ.*, 114(11), 2756–2767, doi:10.1016/j.rse.2010.06.008, 2010.
- 1139 Morris, A., Moholdt, G. and Gray, L.: Spread of Svalbard Glacier Mass Loss to Barents Sea Margins Revealed  
 1140 by CryoSat-2, *J. Geophys. Res. Earth Surf.*, 125(8), doi:10.1029/2019JF005357, 2020.
- 1141 Mouginot, J., Rignot, E. and Scheuchl, B.: Continent-Wide, Interferometric SAR Phase, Mapping of Antarctic  
 1142 Ice Velocity, *Geophys. Res. Lett.*, 46(16), 9710–9718, doi:10.1029/2019GL083826, 2019.

- 1143 Nilsson, J., Vallelonga, P., Simonsen, S. B., Sørensen, L. S., Forsberg, R., Dahl-Jensen, D., Hirabayashi, M.,  
 1144 Goto-Azuma, K., Hvidberg, C. S., Kjaer, H. A. and Satow, K.: Greenland 2012 melt event effects on CryoSat-2  
 1145 radar altimetry, *Geophys. Res. Lett.*, 42(10), 3919–3926, doi:10.1002/2015GL063296, 2015a.
- 1146 Nilsson, J., Sandberg Sørensen, L., Barletta, V. R. and Forsberg, R.: Mass changes in Arctic ice caps and  
 1147 glaciers: implications of regionalizing elevation changes, *Cryosph.*, 9(1), 139–150, doi:10.5194/tc-9-139-2015,  
 1148 2015b.
- 1149 Nilsson, J., Gardner, A., Sørensen, L. S. and Forsberg, R.: Improved retrieval of land ice topography from  
 1150 CryoSat-2 data and its impact for volume-change estimation of the Greenland Ice Sheet, *Cryosphere*, 10(6),  
 1151 2953–2969, doi:10.5194/tc-10-2953-2016, 2016.
- 1152 Nilsson J., Gardner A. S., Paolo F. S.: MEaSURES ITS\_LIVE Antarctic Grounded Ice Sheet Elevation Change,  
 1153 Version 1, "Data archived at National Snow and Ice Data Center", 2021 [DOI registration in progress,  
 1154 temporary access to the data via: [http://its-live-](http://its-live-data.jpl.nasa.gov.s3.amazonaws.com/height_change/Antarctica/Grounded/ANT_G1920V01_GroundedIceHeight.nc)  
 1155 [data.jpl.nasa.gov.s3.amazonaws.com/height\\_change/Antarctica/Grounded/ANT\\_G1920V01\\_GroundedIceHeight](http://its-live-data.jpl.nasa.gov.s3.amazonaws.com/height_change/Antarctica/Grounded/ANT_G1920V01_GroundedIceHeight.nc)  
 1156 [t.nc](http://its-live-data.jpl.nasa.gov.s3.amazonaws.com/height_change/Antarctica/Grounded/ANT_G1920V01_GroundedIceHeight.nc)]
- 1157 Oppenheimer M, B.C. Glavovic , J Hinkel, R van de Wal, A.K Magnan, A Abd-Elgawad, R Cai, M. Cifuentes-  
 1158 Jara, R.M. DeConto, T. Ghosh, J. Hay, F. Isla, B. Marzeion, B. Meyssignac, and Z. S.: Sea Level Rise and  
 1159 Implications for Low-Lying Islands, Coasts and Communities. [online] Available from:  
 1160 [https://www.ipcc.ch/site/assets/uploads/sites/3/2019/11/08\\_SROCC\\_Ch04\\_FINAL.pdf](https://www.ipcc.ch/site/assets/uploads/sites/3/2019/11/08_SROCC_Ch04_FINAL.pdf), 2019.
- 1161 Paolo, F. S., Fricker, H. A. and Padman, L.: Constructing improved decadal records of Antarctic ice shelf height  
 1162 change from multiple satellite radar altimeters, *Remote Sens. Environ.*, 177(May), 192–205,  
 1163 doi:10.1016/j.rse.2016.01.026, 2016.
- 1164 Raney, R. K.: The delay/Doppler radar altimeter, *IEEE Trans. Geosci. Remote Sens.*, 36(5), 1578–1588,  
 1165 doi:10.1109/36.718861, 1998.
- 1166 Richter, A., Popov, S. V., Fritsche, M., Lukin, V. V., Matveev, A. Y., Ekaykin, A. A., Lipenkov, V. Y.,  
 1167 Fedorov, D. V., Eberlein, L., Schröder, L., Ewert, H., Horwath, M. and Dietrich, R.: Height changes over  
 1168 subglacial Lake Vostok, East Antarctica: Insights from GNSS observations, *J. Geophys. Res. F Earth Surf.*,  
 1169 119(11), 2460–2480, doi:10.1002/2014JF003228, 2014.
- 1170 Rignot, E., Mouginot, J., Morlighem, M., Seroussi, H. and Scheuchl, B.: Widespread, rapid grounding line  
 1171 retreat of Pine Island, Thwaites, Smith, and Kohler glaciers, West Antarctica, from 1992 to 2011, *Geophys. Res.*  
 1172 *Lett.*, 41(10), 3502–3509, doi:10.1002/2014GL060140, 2014.
- 1173 Rignot, E., Mouginot, J., Scheuchl, B., van den Broeke, M., van Wessem, M. J. and Morlighem, M.: Four  
 1174 decades of Antarctic Ice Sheet mass balance from 1979–2017, *Proc. Natl. Acad. Sci.*, 116(4), 1095–1103,  
 1175 doi:10.1073/pnas.1812883116, 2019.
- 1176 Roemer, S., Legrésy, B., Horwath, M. and Dietrich, R.: Refined analysis of radar altimetry data applied to the  
 1177 region of the subglacial Lake Vostok/Antarctica, *Remote Sens. Environ.*, 106, 269–284,  
 1178 doi:10.1016/j.rse.2006.02.026, 2007.
- 1179 Schröder, L., Richter, A., Fedorov, D. V., Eberlein, L., Brovko, E. V., Popov, S. V., Knöfel, C., Horwath, M.,  
 1180 Dietrich, R., Matveev, A. Y., Scheinert, M. and Lukin, V. V.: Validation of satellite altimetry by kinematic  
 1181 GNSS in central East Antarctica, *Cryosphere*, 11(3), 1111–1130, doi:10.5194/tc-11-1111-2017, 2017.
- 1182 Schröder, L., Horwath, M., Dietrich, R., Helm, V., van den Broeke, M. R. and Ligtenberg, S. R. M.: Four



- 1183 decades of Antarctic surface elevation changes from multi-mission satellite altimetry, *Cryosph.*, 13(2), 427–449,  
 1184 doi:10.5194/tc-13-427-2019, 2019.
- 1185 Shepherd, A., Ivins, E., Rignot, E., Smith, B., van den Broeke, M., Velicogna, I., Whitehouse, P., Briggs, K.,  
 1186 Joughin, I., Krinner, G., Nowicki, S., Payne, T., Scambos, T., Schlegel, N., A. G., Agosta, C., Ahlström, A.,  
 1187 Babonis, G., Barletta, V., Blazquez, A., Bonin, J., Csatho, B., Cullather, R., Felikson, D., Fettweis, X., Forsberg,  
 1188 R., Gallee, H., Gardner, A., Gilbert, L., Groh, A., Gunter, B., Hanna, E., Harig, C., Helm, V., Horvath, A.,  
 1189 Horwath, M., Khan, S., Kjeldsen, K. K., Konrad, H., Langen, P., Lecavalier, B., Loomis, B., Luthcke, S.,  
 1190 McMillan, M., Melini, D., Mernild, S., Mohajerani, Y., Moore, P., Mouginit, J., Moyano, G., Muir, A., Nagler,  
 1191 T., Nield, G., Nilsson, J., Noel, B., Otsuka, I., Pattle, M. E., Peltier, W. R., Pie, N., Rietbroek, R., Rott, H.,  
 1192 Sandberg-Sørensen, L., Sasgen, I., Save, H., Scheuchl, B., Schrama, E., Schröder, L., Seo, K.-W., Simonsen, S.,  
 1193 Slater, T., Spada, G., Sutterley, T., Talpe, M., Tarasov, L., van de Berg, W. J., van der Wal, W., van Wessem,  
 1194 M., Vishwakarma, B. D., Wiese, D., Wouters, B. and team, T. I.: Mass balance of the Antarctic Ice Sheet from  
 1195 1992 to 2017, *Nature*, 558(7709), 219–222, doi:10.1038/s41586-018-0179-y, 2018.
- 1196 Shepherd, A., Gilbert, L., Muir, A. S., Konrad, H., McMillan, M., Slater, T., Briggs, K. H., Sundal, A. V., Hogg,  
 1197 A. E. and Engdahl, M. E.: Trends in Antarctic Ice Sheet Elevation and Mass, *Geophys. Res. Lett.*, 46(14), 8174–  
 1198 8183, doi:10.1029/2019GL082182, 2019.
- 1199 Shumway, R. H. and Stoffer, D. S.: AN APPROACH TO TIME SERIES SMOOTHING AND  
 1200 FORECASTING USING THE EM ALGORITHM, *J. Time Ser. Anal.*, 3(4), 253–264, doi:10.1111/j.1467-  
 1201 9892.1982.tb00349.x, 1982.
- 1202 Simonsen, S. B. and Sørensen, L. S.: Implications of changing scattering properties on Greenland ice sheet  
 1203 volume change from Cryosat-2 altimetry, *Remote Sens. Environ.*, 190, 207–216, doi:10.1016/j.rse.2016.12.012,  
 1204 2017.
- 1205 Smith, B., Fricker, H. A., Holschuh, N., Gardner, A. S., Adusumilli, S., Brunt, K. M., Csatho, B., Harbeck, K.,  
 1206 Huth, A., Neumann, T., Nilsson, J. and Siegfried, M. R.: Land ice height-retrieval algorithm for NASA’s  
 1207 ICESat-2 photon-counting laser altimeter, *Remote Sens. Environ.*, (November 2018), 111352,  
 1208 doi:10.1016/j.rse.2019.111352, 2019.
- 1209 Smith, B., Fricker, H. A., Gardner, A. S., Medley, B., Nilsson, J., Paolo, F. S., Holschuh, N., Adusumilli, S.,  
 1210 Brunt, K., Csatho, B., Harbeck, K., Markus, T., Neumann, T., Siegfried, M. R. and Zwally, H. J.: Pervasive ice  
 1211 sheet mass loss reflects competing ocean and atmosphere processes, *Science* (80-. ), 5845(April), eaaz5845,  
 1212 doi:10.1126/science.aaz5845, 2020.
- 1213 van Wessem, J. M., van de Berg, W. J., Noël, B. P. Y., van Meijgaard, E., Amory, C., Birnbaum, G., Jakobs, C.  
 1214 L., Krüger, K., Lenaerts, J. T. M., Lhermitte, S., Ligtenberg, S. R. M., Medley, B., Reijmer, C. H., van Tricht,  
 1215 K., Trusel, L. D., van Uft, L. H., Wouters, B., Wuite, J. and van den Broeke, M. R.: Modelling the climate and  
 1216 surface mass balance of polar ice sheets using RACMO2 – Part 2: Antarctica (1979–2016), *Cryosph.*, 12(4),  
 1217 1479–1498, doi:10.5194/tc-12-1479-2018, 2018.
- 1218 Wingham, Ridout, Scharroo, Arthern and Shum: Antarctic elevation change from 1992 to 1996, *Science*,  
 1219 282(5388), 456–8, doi:10.1126/science.282.5388.456, 1998.
- 1220 Wingham, D. J., Rapley, C. G. and Griffiths, H.: New Techniques in Satellite Altimeter Tracking Systems, in  
 1221 Proceedings of the IGARSS Symposium, Zurich, pp. 1339–1344, ESA SP-254, Zurich., 1986.
- 1222 Wingham, D. J., Shepherd, a, Muir, a and Marshall, G. J.: Mass balance of the Antarctic ice sheet., *Philos.*

- 1223 Trans. A. Math. Phys. Eng. Sci., 364(1844), 1627–35, doi:10.1098/rsta.2006.1792, 2006.
- 1224 Wingham, D. J., Wallis, D. W. and Shepherd, A.: Spatial and temporal evolution of Pine Island Glacier
- 1225 thinning, 1995–2006, Geophys. Res. Lett., 36(17), L17501, doi:10.1029/2009GL039126, 2009.
- 1226 Wouters, B., Bamber, J. L., van den Broeke, M. R., Lenaerts, J. T. M. and Sasgen, I.: Limits in detecting
- 1227 acceleration of ice sheet mass loss due to climate variability, Nat. Geosci., 6(8), 613–616,
- 1228 doi:10.1038/ngeo1874, 2013.
- 1229 Wouters, B., Martin-Espanol, A., Helm, V., Flament, T., van Wessem, J. M., Ligtenberg, S. R. M., van den
- 1230 Broeke, M. R. and Bamber, J. L.: Dynamic thinning of glaciers on the Southern Antarctic Peninsula, Science
- 1231 (80-. ), 348(6237), 899–903, doi:10.1126/science.aaa5727, 2015.
- 1232 Zwally, H. J., Giovinetto, M. B., Li, J., Cornejo, H. G. and Beckley, M. a: Mass changes of the Greenland and
- 1233 Antarctica ice sheets and shelves and contributions to sea level rise: 1992-2002, J. Glaciol., 51(175), 509,
- 1234 doi:10.3189/172756505781829007, 2005.
- 1235 Zwally, H. J., Giovinetto, M. B., Beckley, M. A. and Saba, and J. L.: Antarctic and Greenland Drainage
- 1236 Systems, [online] Available from: [http://icesat4.gsfc.nasa.gov/cryo\\_data/ant\\_grn\\_drainage\\_systems.php](http://icesat4.gsfc.nasa.gov/cryo_data/ant_grn_drainage_systems.php), 2012.
- 1237 Zwally, H. J., Li, J., Robbins, J. W., Saba, J. L., Yi, D. and Brenner, A. C.: Mass gains of the Antarctic ice sheet
- 1238 exceed losses, J. Glaciol., 61(230), 1019–1036, doi:10.3189/2015JoG15J071, 2015.
- 1239 Zwally, H. J., Robbins, J. W., Luthcke, S. B., Loomis, B. D. and Rémy, F.: Mass balance of the Antarctic ice
- 1240 sheet 1992–2016: reconciling results from GRACE gravimetry with ICESat, ERS1/2 and Envisat altimetry, J.
- 1241 Glaciol., 67(263), 533–559, doi:10.1017/jog.2021.8, 2021.
- 1242



1243